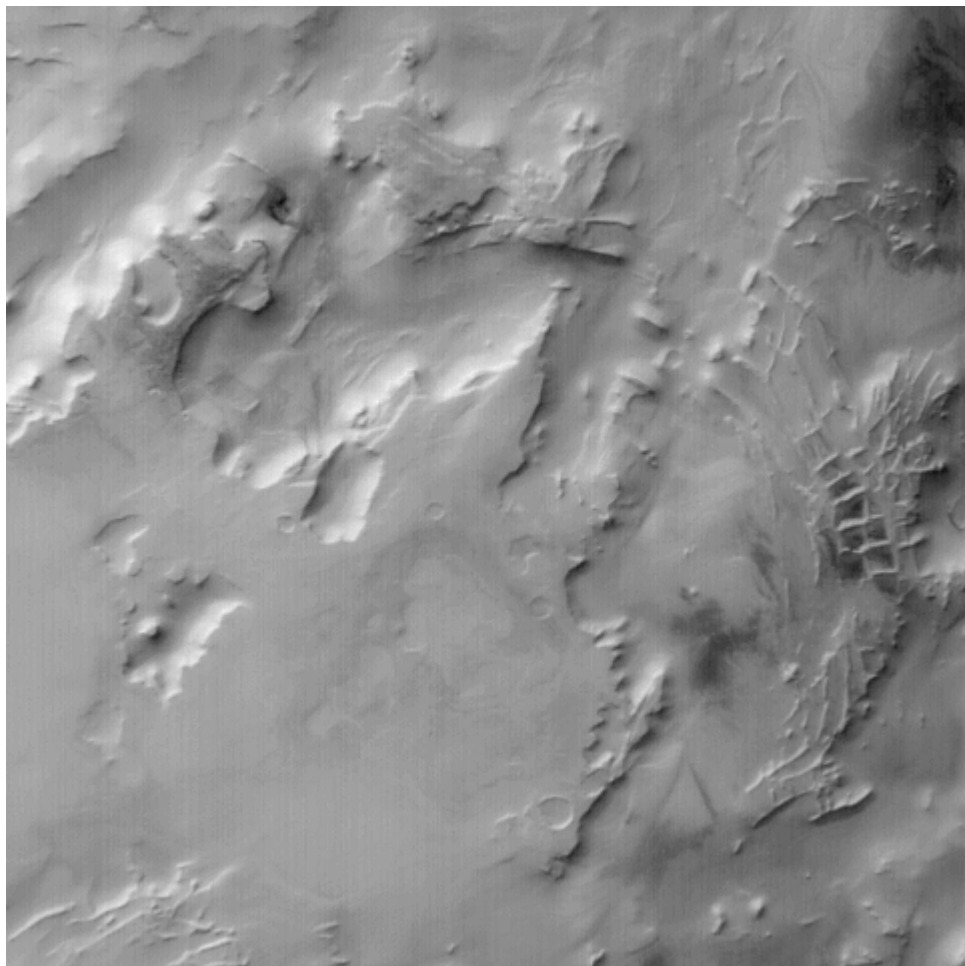


THE “INCA CITY” RIDGE SYSTEM OF MARS

J.H.P. Oosthoek



Submitted as Bachelor Thesis
Faculty of Geosciences, University Utrecht

Date: 29 July 2004

Copies: Ingrid Beekman
Dr K.A.A. Hein

Abstract

The Inca City ridge system is located in the South Polar Region of the planet Mars and consists of sinuous and rectilinear ridges, with some of them forming a rectangular pattern. This research was undertaken to determine whether simple dune formation could explain the Inca City ridges or whether an underlying structure was responsible for the rectilinear pattern. Literature research was undertaken to describe the regional geology of the Inca City ridges. In a Geographical Information System (GIS) a mosaic was created of satellite images of Inca City. Lineaments were created from the mosaic and a lineament analysis resulted in the discovery of a preferred orientation of the Inca City ridges. Four domains of the lineaments were defined. The Inca City ridges were compared to dunes on Earth and it was established that not all the ridges were created by simple dune formation. However the ridges show characteristics of dunes in shape, which, together with the linear trend determined from the lineament analysis, raises the question as to whether the ridges are anchored dunes with an underlying structure responsible for the pattern.

Contents

1. Introduction	7
1.1. Abbreviations	7
2. Regional Geology	9
2.1. Introduction	9
2.2. Regional Stratigraphy	9
2.3. Regional Igneous Activity	12
2.4. Regional Geophysics	12
2.5. Regional Glaciology	13
3. Methodology	15
3.1. Introduction	15
3.2. Input data	15
3.3. Creation of the horizontal and vertical reference files	16
3.4. Orthorectification	17
3.5. Processing the MOC NA slices	19
3.6. Classifying and selecting the MOC NA slices	20
3.7. Creation of the mosaic	20
3.8. Limitations and errors	21
3.9. Lineament Analysis	22
3.10. Profiles	23
4. Results	25
5. Discussion	27
5.1. Introduction	27
5.2. Aeolian dune geometry and formation on Earth	28
5.3. Inca City ridge pattern compared with dune patterns on Earth	29
6. Conclusions	31
Acknowledgements	33
References	35
Internet references	39
Figures	41

Tables	79
Appendices	83
Appendix I	83
Appendix II	84
Appendix III	85

1. Introduction

In the South Polar Region of the planet Mars a landform called Inca City (Sharp, 1973) is located. It consists of sinuous and rectilinear ridges, with some of them forming a rectangular pattern. The rectangular part of Inca City (A on Figure 1.1) consists of two main sinuous, parallel ridges, which are flat-topped and are around 100 meters high with the longest approximately 30 kms in length. The ridges lie approximately 4 kms apart. In between and perpendicular to them, lie ridges that are sharp-crested. A more irregular part of Inca City (B on Figure 1.1) consists of ridges, which form a branching pattern.

The aims of this research have been:

1. To describe the regional geology of Mars focusing on the Inca City ridges.
2. To set up a Geographical Information System (GIS) combining altimetry and image data. The images needed to be georeferenced for accurate scientific results.
3. To determine whether simple dune formation could explain the Inca City ridges or whether an underlying structure may have been responsible for the rectangular pattern.

1.1. Abbreviations

DAF	Dorsa Argentea Formation
DEM	Digital Elevation Model
GCP	Ground Control Point
GIS	Geographical Information System
IAU	International Astronomical Union
LPS	Leica Photogrammetry Suite
MGS	Mars Global Surveyor
MOC	Mars Orbiter Camera
MOLA	Mars Orbiter Laser Altimeter
NA	Narrow Angle
RMS	Root-Mean-Square
SPLD	South Polar Layered Deposits
WA	Wide Angle

2. Regional Geology

2.1. Introduction

The Inca City (Sharp, 1973) landform is located in the Cavi Angusti region of the Martian South Polar region at longitude 64.6°W and latitude 81.5°S. It is situated approximately 80 kms from the permanent South Polar ice cap (Figure 2.1).

The South Polar region has most recently been mapped by Tanaka and Kolb (2001), using Mars Orbiter Laser Altimeter (MOLA) and Mars Orbiter Camera (MOC) data from the Mars Global Surveyor (MGS) orbiter. According to Tanaka and Kolb (2001), Kolb and Tanaka (2002) and Herkenhoff and Plaut (2000), the South Polar region is dominated by three deposits: (1) the Noachian to Early Hesperian aged Plateau Sequence (Table 2.1), (2) the Early to Late Hesperian aged Dorsa Argentea Formation (DAF) which surrounds and stratigraphically underlies about half of the (3) Late Amazonian aged South Polar Layered deposits (SPLD) (Figure 2.2 and 2.3). The SPLD are overlain by the South Polar ice cap, which is approximately 350–400 kms in diameter.

The Cavi Angusti region has been mapped by Tanaka and Kolb (2001) as the Cavi Member of the DAF (Figure 2.4). The term cavi (singular cavus) is defined by the International Astronomical Union (IAU) as irregular steep-sided depressions usually in arrays or clusters.

Inca City is located in the most southern depression of Cavi Angusti (Figure 2.4). Tanaka and Kolb (2001) interpreted the ridges as an esker system caused by basal melting beneath a thick ice sheet, or, clastic dykes linked to the discharge of volatile-rich clastic material. Malin et al. (1998) suggested that the ridges may be mantles of aeolian origin that were lithified by cementation or ice accumulation, with the intervening materials deflated by wind action. They observed that some of their characteristics resemble dunes.

2.2. Regional Stratigraphy

The Noachian to Early Hesperian aged Plateau Sequence was mapped by Tanaka and Scott (1987) as rough, heavily cratered to smooth, relatively flat terrain throughout the

South Polar region. It has been interpreted to consist of lava flows, eolian deposits, pyroclastic material, and impact breccia.

The Early to Late Hesperian aged DAF can be divided in a rugged and knobby materials outcrop (the Rugged Member), 6 plains materials outcrops (the Parva, Argentea, Dorsa, Promethei, Sisyphi and Chasma members) and Cavi Angusti (the Cavi Member) (Figure 2.3) (Tanaka and Kolb, 2001). Crater count and observed superposition of geomorphology were the main methods used in defining the relative chronology of the members, but a distinct geomorphological contact was not always observed (Tanaka and Kolb, 2001).

The Late Amazonian aged SPLD are extensive deposits of layered sedimentary material encircling and underlying the permanent polar ice cap (Murray et al., 2001). The SPLD overlie Early and Late Hesperian material, which implies a stratigraphic hiatus between the Hesperian and Late Amazonian (Fishbaugh and Head, 2001) (Figure 2.3). The Hesperian/Amazonian boundary is estimated to be about 3.3 to 2.9 Gyr ago (Hartmann and Neukem, 2001), ie., Earth equivalent Mid Archean in age. The surface age of the Late Amazonian SPLD, assuming a nominal cratering rate, has been determined to be 14.5 ± 7.2 Ma by Herkenhoff and Plaut (2000), ie. Earth Miocene in age.

The Rugged Member of the DAF, consists of irregular hills, ridges, depressions, and smooth plains (Tanaka and Kolb, 2001). The depressions are tens of meters to a few hundred meters deep and commonly have rims tens of meters high.

The plains members of the DAF have flow-like margins (lobate fronts) and have been interpreted as lava flows (Tanaka and Scott, 1987), or, debris flows (Kolb and Tanaka, 2002). Sinuous, anastomosing ridges occur on the plains members. They have been interpreted to be inverted raised channel topography (Rice and Mollard, 1994), volcanism related features (Tanaka and Scott, 1987), linear dunes (Ruff, 1994), clastic dykes (Ruff and Greeley, 1990), mud ridges caused by mud sheet floods (Jöns, 1992), and eskers (Howard, 1981).

The Cavi Member of the DAF (Figure 2.4) consists of a set of irregular elongated depressions situated in a domed topographic high, referred to as the Angusti Lobe (Ghatan et al., 2003), a quasicircular area with a 550 km diameter. The depressions are up to 1500 m deep with the largest around 100 x 50 km.

Several hypotheses for the formation of the Cavi Angusti region have been proposed in the literature:

- 1) Sharp (1973) proposed aeolian deflation aided by ablation (evaporation) of frozen volatiles, ie. aeolian deflation by the net removal of material by wind processes.
- 2) Basal melting of ground ice (Howard, 1981; Ghatan et al., 2002; Ghatan et al., 2003) where the melting isotherm of an ice cap is raised, resulting in melting at the base (Clifford, 1980).
- 3) Sublimation by katabatic winds from the polar cap (Ghatan et al., 2003).
- 4) Solution of materials resulting in subsidence (Ghatan et al., 2003).

According to Kolb and Tanaka (2001) and Thomas et al. (2000), the SPLD are composed of porous unconsolidated beds consisting of unknown proportions of water ice and dust that have not experienced significant basal melting, or, other glacial-type processes.

The SPLD topography consists of chasmata, scarps and curvilinear troughs. Chasmata (singular chasma) are defined by the IAU as deep, elongated, steep-sided depressions. The largest is Chasma Australis (Figure 2.5) which has been proposed to be formed by katabatic winds modifying a previously existing cap (Howard, 2000), or, by outflow of melt water during heating and partial melting of the polar cap (Clifford, 1987). Dissecting the SPLD are extensive curvilinear troughs (Kolb and Tanaka, 2001). Fishbaugh and Head (2001) interpreted the curvilinear troughs as ablation features. Weijermars (1986) discussed glacial flow as a possible curvilinear trough formation process. Kolb and Tanaka (2001) concluded that wind sculpturing was primarily responsible for forming the chasmata, troughs and scarps.

The South Polar ice cap may principally consist of H₂O ice (Titus et al., 2003), but is covered by CO₂ ice (Paige et al., 1990). The center of the ice cap is offset a few degrees

from the rotational pole (Fishbaugh and Head, 2001). It is dissected by curvilinear troughs (Kolb and Tanaka, 2001).

2.3. Regional Igneous Activity

Tanaka and Scott (1987) identified 6 volcanoes (Figure 2.6) in the South Polar region and three paterae (Figure 2.6). Paterae (singular patera) are defined by the IAU as irregular craters, or complex craters with scalloped edges. The paterae are part of the Early Hesperian aged Amphitrites Formation (Figure 2.3) and were interpreted by Tanaka and Scott (1987) to be circular volcanic centers characterized by concentric and radial wrinkle ridges, and by ring faults.

Seventeen features that were mapped by Tanaka and Scott (1987) as mountains within the DAF located between longitude 020°W and 340°W were re-examined by Ghatan and Head (2002) and interpreted as subglacial volcanoes (A in Figure 2.6). Ghatan et al. (2002, 2003) identified flat-topped mountains and flow-like structures in the Cavi Angusti region, which they interpreted as subglacial volcanoes and lava flows that provided the heat source for basal melting of a larger Hesperian aged ice sheet (B in Figure 2.6). Molinero et al. (2000) investigated a feature originally mapped by Tanaka and Scott (1987) as a mountain and interpreted it to be a basaltic shield volcano (C in Figure 2.6).

2.4. Regional Geophysics

The rough, elevated southern hemisphere of Mars has a relatively featureless gravitational signature, indicating a state of near-isostatic compensation. This suggests that a thick and weak lithosphere exists in the southern hemisphere (Smith et al., 1999). Satellite measurements revealed magnetic lineations in the crust of the Martian southern hemisphere which were interpreted by Connerney et al. (1999) to be formed during plate tectonics and sea floor spreading, analogous to terrestrial oceanic crust. The crustal remnant magnetisation exceeds that of terrestrial crust by more than an order of magnitude.

2.5. Regional Glaciology

An ephemeral CO₂ seasonal polar cap, maximum 1.5 to 2 meters thick (Smith et al., 2001) covers the polar regions of Mars and extends to mid latitudes (Thomas et al., 2000). The CO₂ frost is around 900 kg/m³ which is considerably denser than terrestrial snow (Smith et al., 2001).

Ephemeral dark spots associated with springtime defrosting are found in the SPLD (Bridges et al., 2001), which are interpreted by Kieffer (2003) as CO₂ gas vents. Kieffer (2003) identified ragged channels caused by CO₂ gas venting out with a radially converging dendritic pattern, termed spiders. The dust entrained in the gas is interpreted to fall downwind to form fans. The vents can progress into the dark spots and only the topographic ghost of the vents remains in the summer. The dark spots are interpreted to occur when surface temperatures are close to that of CO₂ sublimation (Bridges et al., 2001). The first surfaces in the southern hemisphere which exhibit spots in the spring are polar dunes. They are also the first to become frosted in the autumn. Horváth et al. (2002) studied the dark spots in the Inca City region and interpreted the sequence of dark spots formation and changes as a result of activity of a kind of probable martian surface organisms.

As in periglacial environments on Earth, polygonal terrains occur in the South Polar region of Mars. They are observed in very young flat regions in high latitudes (Mangold et al., 2002), and have nearly hexagonal geometry and widths of 10 to 30 m.

3. Methodology

3.1. Introduction

To determine whether simple dune formation can explain the Inca City ridges, or, whether an underlying structure is responsible for the rectangular pattern, a Geographical Information System (GIS) was constructed combining altimetry and image satellite data from the Mars Global Surveyor (MGS) orbiter. This involved the creation of an image mosaic from 20 high resolution (3-11 meters/pixel) Mars Orbiter Camera (MOC) Narrow Angle (NA) image slices.

The process of orthorectification was used to create planimetrically true images of the planet's surface, correcting for elevation, a planet's curvature and the orientation and properties of the camera system used. Due to a lack of adequate Ground Control Points (GCPs) the images were georeferenced on top of an MOC Wide Angle (WA) orthophoto reference.

A lineament analysis was performed on the image mosaic. Lineaments were created within ArcMap. This data was used to create a length-weighted Rose Diagram of the lineament orientations.

3.2. Input data

1. Seventy-eight processed, non map-projected MOC NA image slices were acquired from the Malin Space Science Systems (MSSS) MOC Gallery website (www.msss.com/moc_gallery/) each showing parts of Inca City. Appendix I explains how the images were acquired.
2. MOC NA image AB1-07908 showing Inca City with a 15.47 m/pixel resolution was obtained from the MOC Gallery using the method described in Appendix I. This NA image has an unprojected width/height ratio of ~1.45 whereas the other NA images obtained are slices.
3. A 232.5 meter/pixel Mars Orbiter Laser Altimeter (MOLA) Digital Elevation Model (DEM) was obtained from the United States Geological Survey (USGS) Planetary GIS Web Server (<http://webgis.wr.usgs.gov>).

4. A Polar Stereographic projected MOC WA orthophoto mosaic (Mars Digital Image Mosaic version 2.1) of the South Pole was downloaded from the USGS Astrogeology website (<http://astrogeology.usgs.gov/Projects/MDIM21/data/MI90S000E.JPG>).

All the MOC NA images were acquired in a GIF (Graphics Interchange Format) image format and converted to non-compressed TIFF (Tagged Image File Format) images using Adobe Photoshop.

3.3. Creation of the horizontal and vertical reference files

The GIS software product ArcMap 8.3 from ESRI (Environmental Systems Research Institute) was used to create the horizontal reference. The MOC WA orthophoto mosaic was georeferenced on a shaded relief map derived from the MOLA DEM using four GCPs at the centers of craters. The shaded relief map was used because the centers of craters using the MOLA DEM could not be accurately determined. It was made using the ‘Hillshade’ method of the ArcMap ‘Spatial Analyst’ tool. This method involved obtaining the hypothetical illumination of the MOLA DEM by determining illumination values for each pixel. The Hillshade was created using the default settings except for the modeling of shadows.

The orthophoto mosaic was clipped by using the ‘Raster Calculator’ of the Spatial Analyst tool:

1. Inca City was put in the center of the display window of ArcMap.
2. In the ‘Extent’ tab of the ‘Spatial Analyst Options’ window the ‘Analysis extent’ was set to ‘Same as Display’.
3. The Raster Calculator was opened and the orthophoto mosaic was selected.
4. The ‘Evaluate’ button was clicked and a new raster was calculated and saved in an ‘ERDAS IMAGINE’ (IMG) format by right clicking on its name in the Table of Contents window of ArcMap and selecting ‘Make Permanent’.

As a vertical reference the MOLA DEM was used. It was clipped the same way as the orthophoto mosaic except for the ‘Analysis extent’ the clipped orthophoto mosaic was selected. The new calculated raster was saved in an IMG format.

Using the ‘Image Information’ application of the software product ERDAS IMAGINE 8.7, both references had a projection type assigned to them by selecting

Add/Change Projection (Figure 3.1), which opened the ‘Projection Chooser’ window (Figure 3.2) A Stereographic projection was chosen which uses a World Geodetic System (WGS) ’84 Spheroid and Datum. A Polar Stereographic projection was available, but caused errors during the triangulation calculation. WGS 84 was selected because the Leica Photogrammetry Suite (LPS) from Leica Geosystems doesn’t support a spheroid with a radius of Mars and because all the other Spheroids and Datums are deviations from WGS 84. For the ‘latitude of true scale’ 90° S (the geographic South Pole of Mars) was chosen, which is the location on which the projection is centered.

3.4. Orthorectification

For the orthorectification process LPS was used which was formally known as IMAGINE OrthoBASE.

Within the LPS Project Manager a block file was created (Figure 3.3). This opened the Model Setup window where ‘Polynomial-based pushbroom’ and as Geometric Model ‘Generic Pushbroom’ were selected (Figure 3.4). Clicking ‘OK’ opened the Block Property Setup window (Figure 3.5). ‘Set’ was clicked which opened the ‘Projection Chooser’ window. The same projection used for the references was selected (Figure 3.2).

The MOC uses the pushbroom technique in which images are acquired one line at a time (Malin et al., 1991). Each image line is created by an array of sensors each detecting one pixel. A pushbroom camera uses the forward movement of the orbiting spacecraft to build up the image line by line (Lillesand and Kiefer, 1994).

MOC NA AB1-07908 was added to the LPS Project Manager (Figure 3.3) and the orthorectification process for this image was started, which involved three steps:

1. Defining the camera properties (interior orientation) of the image.
2. Creating GCPs (exterior orientation) and performing a triangulation calculation.
3. Resampling the image into an orthorectified image (orthoimage).

To define the interior orientation the Generic Pushbroom Frame Editor window (Figure 3.6) was opened from the Project Manager window (Figure 3.3). In this window the ‘Sensor Information’ window was opened by clicking ‘New’ in the Sensor tab (Figure 3.6). All the parameters were left to their default settings except for the focal length, which was known to be 3500 mm (Malin et al., 1991). In the ‘Model Parameters’ tab the

polynomial order of the sensor model was set to 3 (Figure 3.7), because during a georeferencing tryout in ArcMap, a third order polynomial transformation was needed for the image to best fit the horizontal reference. The orientation of the MOC during acquisition of the image (the Track Incidence angle) and the resolution of the image were entered in the Frame Attributes tab of the Generic Pushbroom Frame Editor window (Figure 3.6). The resolution was obtained from the MOC Gallery download page of AB1-07908. Appendix II shows how the Track Incidence angle was determined.

To create the exterior orientation the Point Measurement window was opened (Figure 3.3). The window allowed for the assigning of GCPs between a reference and an image or the assigning of tie points between two images. The ‘Automatic (x,y) drive’ and ‘Automatic Z value updating’ buttons were activated, the horizontal and vertical reference files were loaded, and ‘Use Viewer As Reference’ was selected (Figure 3.8). The left viewer of the Point Measurement window showed the horizontal reference and the right viewer showed image AB1-07908 (Figure 3.9a).

By clicking ‘Add’, a new GCP was added to the GCP table (Figure 3.9b) in the lower left of the Point Measurement window. A point was created on the horizontal reference by selecting the ‘Create Point’ button (Figure 3.8) and clicking on a ground feature (for example the edge of a ridge) on the reference. A point was created on image AB1-07908 by selecting the ‘Create Point’ button and clicking on the same ground feature on the image, therefore linking the image to the reference and thus creating one GCP. GCPs were created across the image. In the GCP table the ‘Type’ was set to ‘Full’ and ‘Usage’ to ‘Control’ (Figure 3.9b), which defined three-dimensional GCPs using both the horizontal and vertical reference files.

The Triangulation properties window was opened (Figure 3.8 and 3.10). In the ‘General’ tab, ‘Iterations With Relaxation’ was set to 10. The standard for the ‘Iterations With Relaxation’ option is zero but if the quality of the GCPs or sensor information is weak, it is advised to increase this value. In the ‘Advanced Options’ tab ‘Consider Earth Curvature in Calculation’ was selected. Although the curvature of the Planet Mars could not be implemented in the calculation considering the Earth curvature made the calculation the most accurate possible. Next the ‘Run’ button was clicked, which opened the ‘Triangulation Summary’ window. The Root-Mean-Square (RMS) error for image

AB1-07908 was 0.0035045 pixels. The triangulation calculation was accepted by clicking the ‘Accept’ button.

The Point Measurement window was closed and in the LPS Project Manager the Ortho Resampling window was opened (Figure 3.3). In this window a filename was provided and for the X and Y Output Cell sizes, the resolution of AB1-07908 was entered (15.47 m). In the Advanced tab ‘Nearest Neighbor’ was selected as the resampling method. This is a resampling method that transfers original data values without averaging them. After clicking ‘OK’ the new orthoimage was calculated.

Subsequently, the MOC NA slices were orthorectified. Their width projected on the horizontal reference however was only 12-13 pixels, which did not allow for accurate GCPs to be collected. Using the AB1-07908 orthophoto on top of the MOC WA mosaic, as the horizontal reference for the MOC slices, was not possible because a two-layer horizontal reference could not be used within LPS.

Creating a new raster consisting of the MOC WA mosaic and the AB1-07908 orthophoto was also attempted using the Raster Calculator of ArcMap. This raster would have the same extent of the former but the resolution of the latter. This was not possible because the Raster Calculator does not permit a new raster larger than the smallest extent to be created, which was AB1-07908. Therefore it was decided to georeference the MOC NA slices in ArcMap with the MOC WA mosaic and orthophoto AB1-07908 as references. The horizontal reference and the AB1-07908 orthophoto had a Mars South Polar Stereographic projection (Table 3.1) assigned via ArcCatalog from ESRI and were loaded into ArcMap. They provided the GIS reference basis on which the mosaic of MOC NA slices was constructed.

3.5. Processing the MOC NA slices

1. Twenty slices were processed using a contrast enhancement procedure (Figure 3.11).
2. Distortion and non-image data was removed in 21 slices.
3. Eleven slices observed gaps caused by a temporary stop during image acquisition. This gap causes spatial misalignment of the parts of the image above and below the gap. These parts therefore were defined as separate images and named

<imagename>-<number>. For example, image E0902162 was broken up into two parts, the upper part E0902162-1 and the lower part E0902162-2 (upper and lower refer to image space and not map space).

4. Four images were found unusable because they resolved too much image distortion, or because of a lack of GCPs.

3.6. Classifying and selecting the MOC NA slices

The resolution, orientation and location data of the MOC NA slices was manually imported into Microsoft Excel from the MOC Gallery download page of each image (Figure 3.12). This revealed image resolutions between 1.4 and 11 m/pixel with an average resolution of 4.2 m/pixel.

The orientations provided for each image slice in the ancillary data are defined as the angle in degrees clockwise from a line drawn from the center, to the right edge of the image, to the direction of the North Pole of Mars. Importing these values into Excel revealed two distinct image orientations. This allowed for the division of the image slices into two groups. Group A consists of 51 images with an orientation of $\sim 110^\circ$ and Group B consists of 31 images with an orientation of $\sim 251^\circ$.

The location of the images was plotted in ArcMap. The latitude and longitude coordinates were first transformed into the Cartesian coordinates of the South Polar Stereographic projection in Excel using cosine and sine functions, and imported in ArcMap. Appendix III explains this procedure in more detail.

Twenty-nine overlapping images were observed at 12 different locations. Not all of these images were used weighing between the largest extent and the largest resolution.

3.7. Creation of the mosaic

Twenty of the initial 87 MOC NA image slices were selected for the mosaic, 16 from Group A and 4 from Group B (Table 3.2). The Group A images were georeferenced, which resulted in 16 parallel-aligned images and subsequently the 4 images from Group B were georeferenced. All the slices were georeferenced using a first order transformation. A higher order transformation was not attempted because these transformations need more accurate GCPs compared to the first order transformation.

However these were only available on orthoimage AB1-07908, so that, using higher order transformation would have resulted in less precision. When slices that only partly overlay orthoimage AB1-07908 were georeferenced onto AB1-07908, they fitted well to this image but not to the MOC WA mosaic, and the farther away from AB1-07908, the larger the offset. Therefore only one or two GCPs per slice were used to georeference the slices on the MOC WA mosaic. Outside AB1-07908, already georeferenced slices were also used as a reference for other slices.

3.8. Limitations and errors

1. MOC NA image AB1-07908 was taken during the aerobraking phase of the MGS mission. Aerobraking means that the spacecraft uses the friction with the atmosphere to slow down. The image was taken from an altitude of 3222.87 km whereas all the MOC NA slices used were taken from an altitude of ~370 km. The camera was orientated obliquely to the planet surface during acquisition. Therefore image AB1-07908 deviates from ideal when compared to an image acquired when the camera is focused perpendicular to the mean planet surface. However, the image is the only available which covers approximately the half of Inca City with a 15.47 m/pixel resolution.
2. The MOC NA images were georeferenced using a first order transformation, which resulted in an average weighed RMS error of ~88.1 meters (taking the amount of GCPs per image into account).
3. The United States Geological Survey developed a software package named Integrated Software for Imagers and Spectrometers (ISIS) for processing, analysing, and displaying remotely sensed image data. This allows for much easier image acquisition by location compared to the method used for this research.
4. The ‘Polynomial-based pushbroom’ Sensor Model did not include the elevation of the MGS orbiter during acquisition in the triangulation calculation.
5. The MOC NA mosaic does not cover 100% of Inca City (Figure 3.13).

3.9. Lineament Analysis

A new Shape-file was created within ArcCatalog with the ‘Feature Type’ set to ‘Polyline’. This file was loaded into ArcMap with the mosaic as background. The ‘Editor’ of ArcMap was started and as Task ‘Create 2-Point Line Features’ was selected. Using the ‘Sketch Tool’ lines were drawn on the mosaic and when finished the edit was saved. The X and Y locations of both end-points needed to be extracted from the Shape-file. This was accomplished by converting the Shape-file within ArcCatalog into a Coverage-file. The Coverage-file had a Geographical projection assigned with ‘WGS 1984’ as a Spheroid and was converted within ArcToolbox into a MOSS-file. This file type provided the necessary X and Y locations of the two end-points of each lineament. The file was imported in Microsoft Excel, where the X and Y locations of the two end-points were used to calculate the orientation and length of each lineament. The reference used for the angles, was the zero degree longitude (the Martian Prime Meridian) and the angle increased counterclockwise.

In Excel the lineament orientation and lineament length columns were selected and copy-pasted in a text file. The software program GEORient 9.2 was started and the Rose Diagram button was selected (Figure 3.14). The text file was selected which opened the ‘File structure and data conventions’ window (Figure 3.15). In the ‘Plot as’ tab the ‘Primary data set’ was set to Directions and in the ‘Appended Data’ tab ‘Numeric value’ was selected and set to Length (Figure 3.15). In the ‘Plot as’ tab the Lines button was pressed. This opened a new window in which the ‘Rose Type’ was set to ‘Length – Azimuth’ and the GO button was pressed (Figure 3.16). This created a length-weighted Rose Diagram (Figure 4.2).

In ArcMap the lineaments were divided in four domains, which were created by exporting the Shape-file containing all the lineaments into 4 new Shape-files. For each new domain Shape-file the ‘Editor’ was used to delete the lineaments outside the domain. A length-weighted Rose Diagram was created for each domain Shape-file using the method described above.

3.10. Profiles

A new MOLA DEM became available during the research with a ~114 m/p resolution. To create a profile using the ‘3D Analyst’ tool from ArcMap the following steps were taken (Figure 3.17):

1. Within the ‘3D Analyst’ tool ‘Layer’ was set to the ~114 m/p MOLA DEM.
2. A line was drawn onto the MOLA DEM in the display window of ArcMap using the ‘Interpolate Line’ button.
3. The ‘Create Profile Graph’ button was selected.

4. Results

1. A mosaic was created from 20 MOC NA image slices (Figure 4.1).
2. Lineaments were created from the MOC NA mosaic (Figure 4.2).
3. A length-weighted Rose Diagram was created (Figure 4.3) from the lineaments. The Rose Diagram shows one ordinate Principal Direction (PD1) of $\sim 110^\circ$ - 290° and three subordinate Principal Directions (PD2 to 4) of $\sim 85^\circ$ - 265° , $\sim 65^\circ$ - 245° and $\sim 35^\circ$ - 215° respectively.
4. Four lineament domains were defined (Figure 4.4) and for each a length-weighted Rose Diagram was created (Figures 4.5 to 4.8).
5. Domain A shows a preferred orientation of $\sim 70^\circ$ - 250° , between PD2 and PD3 (Figure 4.5).
6. Domain B shows an ordinate preferred orientation of $\sim 35^\circ$ - 215° , approximately corresponding with PD4, and a subordinate preferred orientation of $\sim 110^\circ$ - 290° , approximately corresponding with PD1 (Figure 4.6).
7. Domain C shows an ordinate preferred orientation of $\sim 115^\circ$ - 295° , approximately corresponding with PD1, and a subordinate preferred orientation of $\sim 25^\circ$ - 205° , which is approximately perpendicular to the ordinate preferred orientation (Figure 4.7).
8. Domain D shows an ordinate preferred orientation of $\sim 95^\circ$ - 275° and a subordinate preferred orientation of $\sim 65^\circ$ - 245° , approximately corresponding to PD3 (Figure 4.8).
9. A length-weighted Rose Diagram was created of all Inca City lineaments except Domain A (Figure 4.9). This shows an ordinate preferred orientation of $\sim 110^\circ$ - 290° , corresponding to PD1 and a subordinate preferred orientation of $\sim 35^\circ$ - 215° corresponding to PD4. The orientation of the Domain A ridges differ by approximately 40 degrees from PD1 (Figures 4.5 and 4.9).
10. Profiles were created of a selection of Inca City ridges (Figure 4.10).
11. A linear trend was observed in the lineaments (Figure 4.11).

5. Discussion

5.1. Introduction

This research was undertaken to determine whether simple dune formation could explain the Inca City ridges, or, whether an underlying structure was responsible for the rectilinear pattern.

Inca City lies in the Cavi Angusti region of the Martian South Polar Region. Several hypotheses for the formation of Cavi Angusti have been proposed:

1. Sharp (1973) proposed aeolian deflation aided by ablation (evaporation) of frozen volatiles, ie. aeolian deflation by the net removal of material by wind processes.
2. Basal melting of ground ice (Howard, 1981; Ghatan et al., 2002; Ghatan et al., 2003) where the melting isotherm of an ice cap is raised, resulting in melting at the base (Clifford, 1980).
3. Sublimation by katabatic winds from the polar cap (Ghatan et al., 2003).
4. Solution of materials resulting in subsidence (Ghatan et al., 2003).

Aeolian deflation is caused by wind, which, logically would have been active across the entire South Polar Region of Mars, and not bounded by Cavi Angusti itself. Therefore aeolian deflation does not of itself solve the question as to why Cavi Angusti is easier to erode than the surrounding area.

Basal melting of ground ice implies that a glacier once overlay the Cavi Angusti region. A thermal trigger, for example an intrusion from below, or a sediment blanket on top of the glacier could cause the basal melting.

Sublimation by katabatic winds from the polar cap does not solve the question as to why Cavi Angusti is more erosive than the surrounding area. The solution of materials resulting in subsidence hypothesis does not state the cause of the solution.

It is most probable that a mix of processes, perhaps all four hypotheses, perhaps working at different time periods, caused the formation of the Cavi Angusti basin. The Inca City ridges have been interpreted by Tanaka and Kolb (2001) as an esker system caused by basal melting beneath a thick ice sheet, or, clastic dykes linked to the discharge of volatile-rich clastic material. Malin et al. (1998) suggested that the ridges may be mantles of aeolian origin that are lithified by cementation or ice accumulation,

with the intervening materials deflated by wind action. They observed that some of their characteristics resemble dunes. I will consider the Inca City architecture in terms of aeolian dunes.

5.2. Aeolian dune geometry and formation on Earth

The formation of dunes has been discussed by Livingstone and Warren (1996) and Hersen et al. (2002). Aeolian dunes are deposits of windblown material, which can be sand, gypsum, salt crystals or ice. They mainly occur in arid regions or as shore dunes, and are defined as features between 0.3 m and 400 m high and between 1 m and 500 m wide. They are continuously reshaped by the wind. The wind sets the material in motion and thus changes the shape of the dune. Reciprocally, the dune is large enough to modify the flow pattern of the wind. The equilibrium between the two leads to the selection of shape and dynamics of dunes.

Aeolian dune formation is initiated when particle-saturated air comes into contact with irregularities on the ground surface or small obstacles like plants, which cause deposition. Survival of a patch of deposited material depends on the achievement of a minimum size, which is dependent of the material supply.

A common characteristic of dunes is replication, that is, the development of successive dunes all of roughly the same form, and with a regular spacing. No conclusive hypotheses explain this type of dune behaviour.

Aeolian dunes can be divided into two groups, free dunes and anchored dunes. Anchored dunes develop because material is immobilised by vegetation or topographic obstructions and free dunes develop without these obstructions.

Four types of free dunes have been classified by basis of dune form: transverse, linear, star and sheet dunes. They can be separated by the occurrence and properties of slip faces and the net transport direction (Table 1). By plotting wind direction variability against the amount of sand supply a distinction can be made between transverse, linear and star dunes (Figure 5.1).

The cross-sectional profile of a simple dune that is formed in a unimodal wind regime is asymmetric. It has a windward slope and a lee slope (Figure 5.2a). The lee slope is formed by material that falls over the brink (Figure 5.2a) causing avalanches and slumps

on the lee slope. The crest is the highest point of the dune, which can be the same as the brink (Figure 5.2a and b). Because of wind erosion and deposition, dunes slowly move downwind (Figure 5.2c).

Linear dunes do not have a distinct windward and lee slope and have been hypothesised to be formed by a bimodal wind regime or by thermally induced roll-vortices (Figure 5.3).

5.3. Inca City ridge pattern compared with dune patterns on Earth

The basin in which Inca City lies has been mapped by Tanaka and Kolb (2001) as the Hesperian aged DAF Cavi Member. The Inca City ridges are surrounded by Amazonian aged SPLD material (Figure 2.4c). This raises the question if the Inca City ridges could be aeolian dunes.

The Inca City ridges agree in height with mega-dunes on Earth. Mega-dunes in the Badain Jaran Desert, China, have a general height of approximately 150 to 350 m with the highest dune over 400 m high (Dong et al., 2004). Megadunes in Liwa, Ar Rub' Al Khali, United Arab Emirates are between 40 and 160 m high, with the average height around 110 m (El-Sayed, 2000). No terrestrial mega-dunes have been observed resembling the Inca City ridge pattern.

A cross-section of the Inca City ridges does not reveal the presence of a windward and lee slope (Figure 4.10), which agrees with terrestrial linear dune shapes, although the ~114 m/p resolution of the MOLA DEM may be insufficient. In Domain C the long ridges are round crested and the smaller perpendicular ridges are sharp crested. Some of the sharp crested ridges show a smooth curved crest (Figure 5.4). The occurrences of slumps and avalanches on the ridge slopes are not apparent in the images.

Of all terrestrial dune patterns studied in the literature those that best resemble the Inca City ridge pattern are described by Bullard et al. (1995). They identified 5 dune classes in an area of 4000 km² in the southwestern Kalahari dunefield, Africa. Class 4 shows a resemblance with the Inca City ridge pattern (Figure 4.1 and 5.4) and is described as a linear dune network comprising large steep dunes and smaller gently sloping dunes. Larger dunes have broadly linear trend but are very sinuous. Small dunes tend to be orientated perpendicular to this trend.

The Kalahari Desert research site is 4000 km² and is covered with linear dunes of the 5 different dune classes. The Class 4 pattern in the Kalahari Desert is a relatively small-scale example of a pattern, which is replicated on a larger scale. Inca City is approximately 3000 km² and unique in the South Polar Region of Mars. The linear dunes of the Kalahari Desert are between 8 and 16 m high, whereas the Inca City ridges are between ~50 and ~300 m high.

The longest sinuous linear dunes of the Class 4 pattern are observed to have a preferred orientation caused by the dominant wind direction (Figure 5.5), which agrees with the occurrence of the preferred orientation PD1 of the Inca City ridges (Figure 4.3). The pattern however varies within the boundaries of the Inca City ridge system, where the four lineament domains all have different preferred orientations (Figures 4.5 to 4.8).

Domain A resembles a combination of classes 1 and 3, but does not connect in a streaming manner with Domain C, which would have to be the case if the ridges were linear dunes. The longest lineaments of Domains B, C and D, together with other ridges in the vicinity, form a circular pattern (Figure 5.6), with the longest ridges of Inca City varying approximately 90 degrees in orientation.

Y-junctions of the longest linear dunes in the Kalahari linear dune network occur in the Inca City ridge system (Figure 4.2). They do not occur in Domains B and D and are not orientated approximately in the same direction, which would be expected if the Inca City ridges were linear dunes.

Regarding the Inca City ridge pattern it is unlikely that all the ridges are created by simple dune formation resulting in free dunes. They however show characteristics of dunes in shape, which, together with the linear trend observed in the lineaments (Figure 4.11) suggests that the ridges could be anchored dunes with an underlying structure responsible for the pattern.

6. Conclusions

The Inca City ridge system has a preferred orientation PD1 (Figure 4.3). The system was divided in four domains, each showing different preferred orientations (Figures 4.5 to 4.8). A linear trend was observed in the ridge lineaments (Figure 4.11).

The Inca City ridge system was compared with dunes on Earth. The height of the ridges is not uncommon for terrestrial mega-dunes. However the Inca City ridge pattern has not been observed in terrestrial mega-dunes. One pattern of linear dunes in the Kalahari Desert showed a resemblance to the Inca City ridge pattern (Figure 4.1 and 5.4). The Kalahari linear dune pattern however is replicated on a larger scale whereas Inca City is unique in the South Polar Region of Mars. The Inca City ridges are on average 15 times higher than the Kalahari linear dunes. The difference of preferred orientations in the four domains of Inca City would not be expected if the ridges were linear dunes. Therefore it is unlikely that all the ridges are created by simple dune formation resulting in free dunes. They however show characteristics of dunes in shape, which, together with the linear trend observed in the lineaments (Figure 4.11) suggests that the ridges could be anchored dunes with an underlying structure responsible for the pattern.

Acknowledgements

The author acknowledges the use of Mars Orbiter Camera images processed by Malin Space Science Systems that are available at http://www.msss.com/moc_gallery/. Thanks are extended to Dr K.A.A. Hein as my supervisor, to T. Hare from the USGS for the Stereographic MOLA DEM and to M. Zeylmans van Emmichoven of the GIS department for the advice concerning the GIS.

References

- Allaby, A., Allaby, M., 1999. Dictionary of Earth Sciences, Oxford University Press.
- Bridges, N.T., Titus, T.N., Herkenhoff, K.E., Kieffer, H.H., Hecht, M.H., Mercer, C., 2001. Seasonal Dark Spots in Martian gullies and other terrains studied by TES and other data sets. Exploring Mars with TES: A Data User's Workshop (See: <http://tes.asu.edu/TESworshop/>), Arizona State University.
- Bullard, J.E., Thomas, D.S.G., Livingstone, I., Wiggs, G.F.S., 1995. Analysis of linear sand dune morphological variability, southwestern Kalahari Desert. Geomorphology 11, 189-203.
- Clifford, S.M., 1980. Mars: Polar Cap Basal Melting as a Recharge Mechanism for a Global Groundwater System. Lunar and Planetary Science Conference XI. 165-167.
- Clifford, S.M., 1987. Polar basal melting on Mars. Journal of Geophysical Research 92, 9135–9152.
- Connerney, J.E.P., Acuña, M.H., Wasilewski, P.J., Ness, N.F., Rème, H., Mazelle, C., Vignes, D., Lin, R.P., Mitchell, D.L., Cloutier, P.A., 1999. Magnetic lineation in the ancient crust of Mars. Science 284, 794-798.
- Dong, Z., Wang, T., Wang, X., 2004. Geomorphology of the megadunes in the Badain Jaran Desert. Geomorphology 60, 191–203.
- El-Sayed, M.I., 2000. The nature and possible origin of mega-dunes in Liwa, Ar Rub' Al Khali, UAE. Sedimentary Geology 134, 305-330.
- Fishbaugh, K.E., Head III, J.W., 2001. Comparison of the North and South Polar Caps of Mars: New Observations from MOLA Data and Discussion of Some Outstanding Questions. Icarus 154, 145–161.
- Ghatan, G.J., Head III, J.W., 2002. Candidate subglacial volcanoes in the south polar region of Mars: Morphology, morphometry, and eruption conditions. Journal of Geophysical Research 107, No. E7, 10.1029/2001JE001519.
- Ghatan, G.J., Head III, J.W., Pratt, S., 2002. Cavi Angusti, Mars: Evidence For Volcanic Activity, Ice Sheet Melting, And Basal Drainage Of Water. Lunar and Planetary Science Conference 33rd, Abstract 1054.

- Ghatan G.J., Head III, J.W., Pratt, S., 2003. Cavi Angusti, Mars: Characterization and assessment of possible formation mechanisms. *Journal of Geophysical Research* 108, No. E5, 5045.
- Hartmann, W.K., Neukem, G., 2001. Cratering Chronology and the Evolution of Mars. *Space Science Reviews* 96, 165-194.
- Herkenhoff, K.E., Plaut, J.J., 2000. Surface Ages and Resurfacing Rates of the Polar Layered Deposits on Mars. *Icarus* 144, 243-253.
- Hersen, P., Douady, S., Andreotti, B., 2002. Relevant Length Scale of Barchan Dunes, *Physical Review Letters* Vol. 89, Number 26, 264301(1 - 4).
- Horváth, A., Bérczi, S., Gánti, T., Gesztesi, A., Szathmáry, E., 2002. The "Inca City" Region Of Mars: Testfield For Dark Dune Spots Origin. *Lunar and Planetary Science Conference* 33rd, Abstract 1109.
- Howard, A.D., 1981. Etched plains and braided ridges of the south polar region of Mars: Features produced by basal melting of ground ice? *NASA Technical Memorandum* 84211, 286-288. National Aeronautics and Space Administration, Washington, DC.
- Howard, A.D., 2000. The Role of Eolian Processes in Forming Surface Features of the Martian Polar Layered Deposits. *Icarus* 144, 267–288.
- Jöns, H.P., 1992. Fossil glaciations in the environs of the South Pole, Mars? *Lunar and Planetary Science Conference* 23th, 633-634.
- Kieffer, H.H., 2003. Behavior of solid CO₂ on Mars: A real zoo. *Sixth International Conference on Mars*. Abstract 3158.
- Kolb, E.J., Tanaka, K.L., 2001. Geologic History of the Polar Regions of Mars Based on Mars Global Surveyor Data: II. Amazonian Period. *Icarus* 154, 22-39.
- Kolb, E.J., Tanaka, K.L., 2002. Non-glacial interpretations of long-term Mars South Polar volatile history based on MGS data and new geologic mapping. *Lunar and Planetary Science Conference* 33rd, Abstract 2003.
- Lillesand, T.M., Kiefer, R.W., 1994. *Remote Sensing and Image Interpretation*. John Wiley and Sons, Inc.
- Livingstone, I., Warren, A., 1996. *Aeolian Geomorphology: An Introduction*, Addison Wesley Longman Limited.

- Malin, M.C., Carr, M.H., Danielson, G.E., Davies, M.E., Hartmann, W.K., Ingersoll, A.P., James, P.B., Masursky, H., McEwen, A.S., Soderblom, L.A., Thomas, P., Veverka, J., Caplinger, M.A., Ravine, M.A., Soulanille, T.A., Warren, J.L., 1998. Early Views of the Martian Surface from the Mars Orbiter Camera of Mars Global Surveyor. *Science* 279, 1681-1685.
- Malin, M.C., Danielson, G.E., Ravine, M.A., Soulanille, T.A., 1991. Design and Development of the Mars Observer Camera. *International Journal of Imaging Systems and Technology*, Vol. 3, 76-91.
- Malin, M.C., Edgett, K.S., Carr, M.H., Danielson, G.E., Davies, M.E., Hartmann, W.K., Ingersoll, A.P., James, P.B., Masursky, H., McEwen, A.S., Soderblom, L.A., Thomas, P., Veverka, J., Caplinger, M.A., Ravine, M.A., Soulanille, T.A., Warren, J.L., 2003. Mars 2003, NASA's Planetary Photojournal (<http://photojournal.jpl.nasa.gov/>), PIA04591.
- Malin, M.C., Edgett, K.S., Davis, S.D., Caplinger, S.D., Jensen, E., Supulver, K.D., Sandoval, J., Posiolova L., Zimdar, R., 2000. AB1-07908, Malin Space Science Systems Mars Orbiter Camera Image Gallery (http://www.msss.com/moc_gallery/).
- Mangold, N., Forget, F., Costard, F., Peulvast, J., 2002. High Latitude Patterned Grounds On Mars: Evidence For Recent Melting Of Near-surface Ground Ice. *Lunar and Planetary Science Conference* 33rd, Abstract 1219.
- Molinero, R.J., Garvin, J.B., Sakimoto, S.E.H., 2000. Mars Orbiter Laser Altimeter (MOLA) topography and preliminary analysis of a South Polar enigmatic small volcano. *31st Lunar and Planetary Science Conference*, Abstract 1895.
- Murray, B., Koutnik, M., Byrne, S., Soderblom, L., Herkenhoff, K., Tanaka, K.L., 2001. Preliminary Geological Assessment of the Northern Edge of Ultimi Lobe, Mars South Polar Layered Deposits. *Icarus* 154, 80–97.
- Paige, D., Herkenhoff, K., Murray, B., 1990. Mariner 9 observations of the south polar cap of Mars: Evidence for residual CO₂ frost. *Journal of Geophysical Research* 95, 1319-1335.
- Rice Jr., J.W., Mollard, J.D., 1994. Analogs and interpretations for the martian thumbprint terrain and sinuous ridges. *Proceedings of the Lunar and Planetary Science Conference* 25th, 1127-1128.

- Ruff, S., Greeley, R., 1990. Sinuous ridges of the South Polar region, Mars: possible origins. *Lunar and Planetary Science Conference 21st*, 1047-1048.
- Ruff, S.W., 1994. Comparison of Mars sinuous ridges with terrestrial linear dunes: Observations from the field. *Proceedings of the Lunar and Planetary Science Conference 25th*, 1171–1172.
- Sharp, R.P., 1973. Mars: South polar pits and etched terrain. *Journal of Geophysical Research* 78, 4222-4230.
- Smith, D.E., Sjogren, W.L., Tyler, G.L., Balmino, G., Lemoine, F.G., Konopliv, A.S., 1999. The Gravity Field of Mars: Results from Mars Global Surveyor. *Science* 286, 94-97.
- Smith, D.E., Zuber, M.T., Neumann, G.A., 2001. Seasonal Variations of Snow Depth on Mars. *Science* 294, 2141-2146.
- Tanaka, K.L., Scott, D.H., 1987. Geologic Map of the Polar Regions of Mars. U.S. Geological Survey Miscellaneous Investigation Map I-1802-C.
- Tanaka, K.L., Kolb, E.J., 2001. Geologic History of the Polar Regions of Mars Based on Mars Global Surveyor Data: I. Noachian and Hesperian Periods. *Icarus* 154, 3-21.
- Thomas, P.C., Malin, M.C., Edgett, K.S., Carr, M.H., Hartmann, W.K., Ingersoll, A.P., James, P.B., Soderblom, L.A., Veverka, J., Sullivan, R., 2000. North-south geological differences between the residual polar caps on Mars. *Nature* 404, 161-164.
- Titus, T.N., Kieffer, H.H., Christensen, P.R., 2003. Exposed Water Ice Discovered near the South Pole of Mars. *Science* 299, 1048 - 1051.
- Weijermars, R., 1986. The polar spirals of Mars may be due to glacier surges deflected by Coriolis forces. *Earth and Planetary Science Letters* 76, 227–240.

Internet references

How to create orthophotos with Erdas Imagine Orthobase 8, <http://www.wsl.ch/staff/jesse.kalwij/phd/Protocol/welcome-en.ehtml>.

IMAGINE OrthoBASE Frequently Asked Questions, http://www.esrij.com/products/imagine_addon/OrthoBASE_FAQs.pdf. ESRI Japan.

Importing XY (Point) Data from MS Excel to ArcMap, <http://www.biology.ualberta.ca/facilities/gis/uploads/instructions/AVXYData.pdf>. Biological Sciences, University of Alberta, Canada, 2002.

Law of Cosines, <http://mathworld.wolfram.com/LawofCosines.html>, Mathworld.

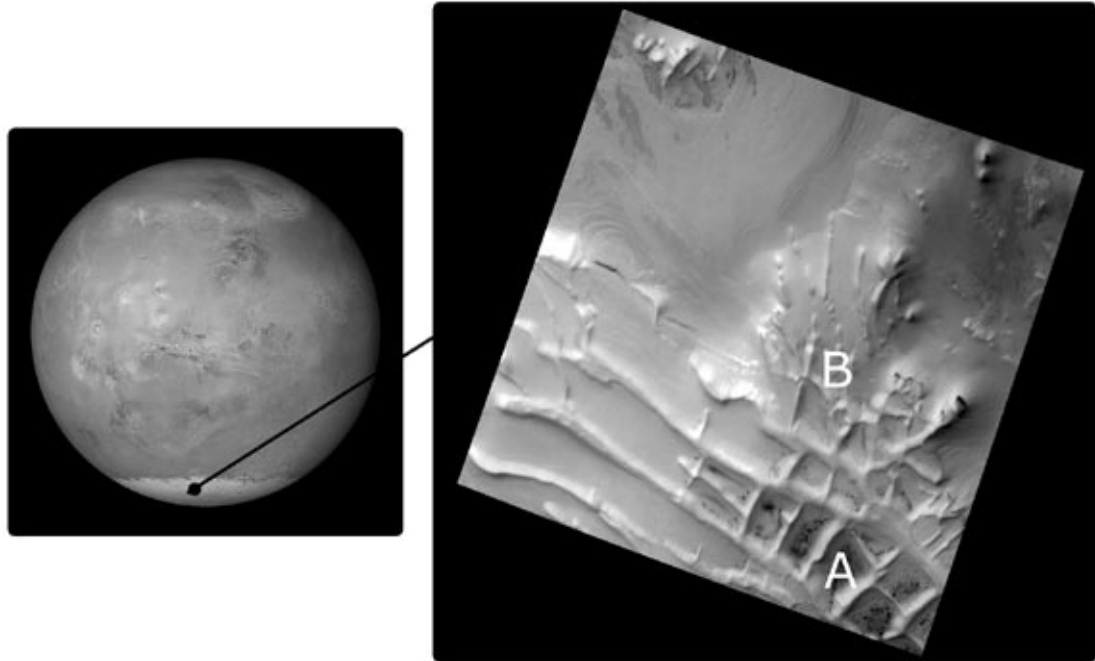
Figures

Figure 1.1. Location of the Inca City ridges, Mars. (Images credit: NASA/JPL/Malin Space Science Systems)

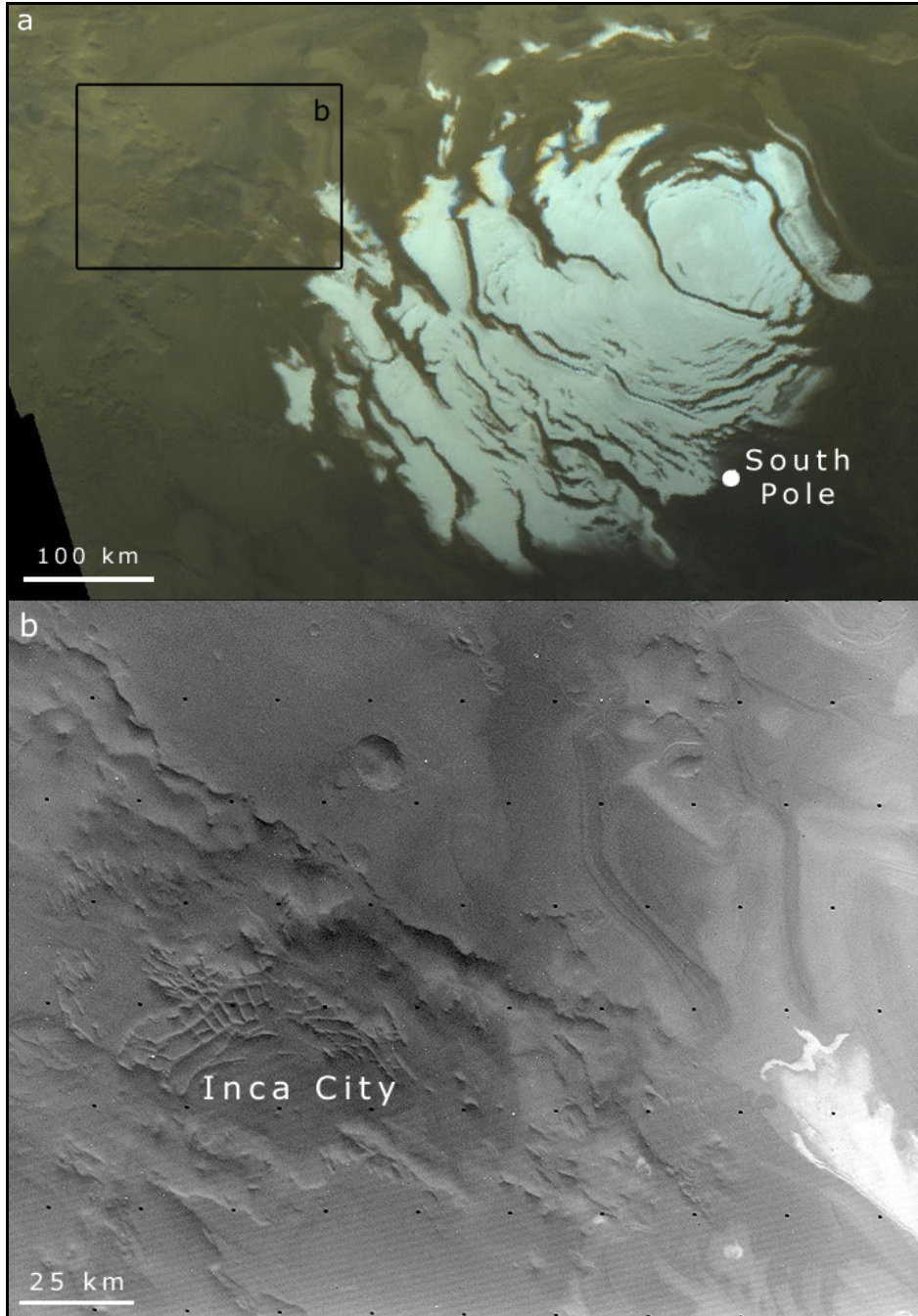


Figure 2.1. The location of the Inca City landform relative to the permanent CO₂ ice cap and the rotational South Pole of Mars. **a.** Redrawn after Viking 2 Orbiter image number MG90S000-407B. **b.** Redrawn after Viking 2 Orbiter image number 421B64.

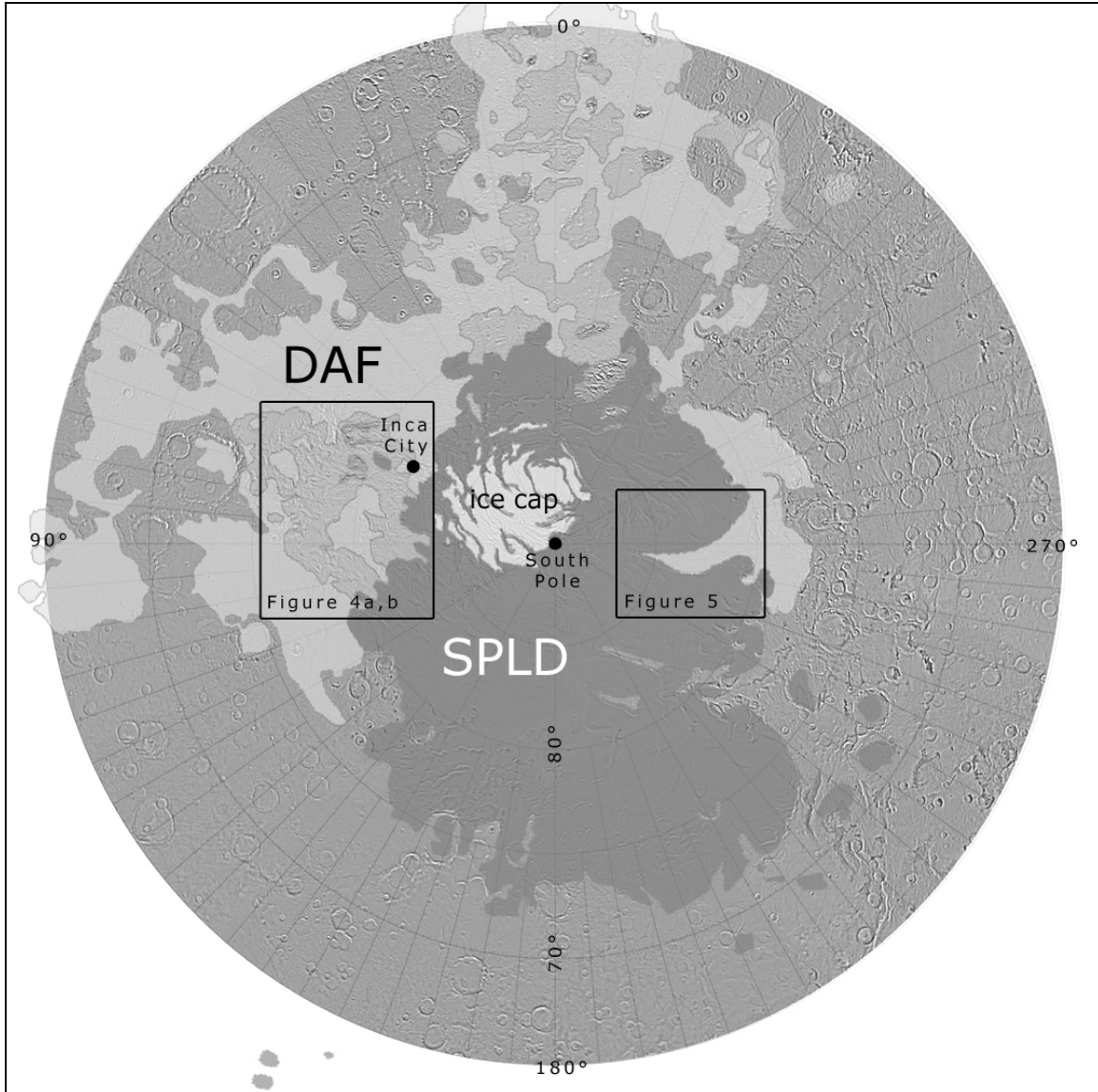


Figure 2.2. MOLA derived image of the South Polar region of Mars showing the Dorsa Argentea Formation (DAF) and the South Polar Layered Deposits (SPLD) mapped by Tanaka and Scott (1987). The darker gray unit within the DAF has been mapped by Tanaka and Scott (1987) as undivided Hesperian or Noachian aged material.

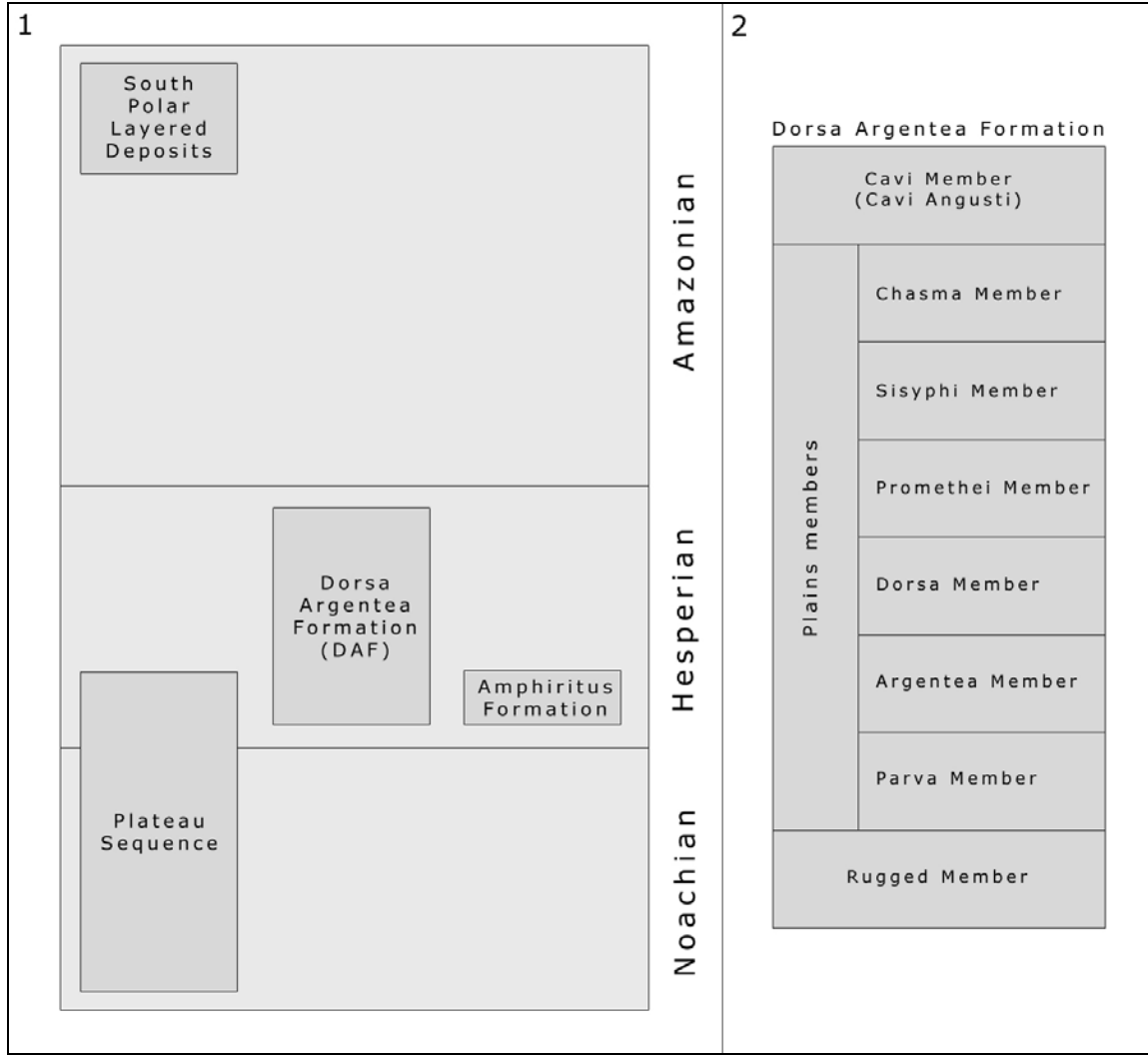


Figure 2.3. Stratigraphical columns of (1) the South Polar region, Mars, (2) the Dorsa Argentea Formation. After Tanaka and Kolb (2001).

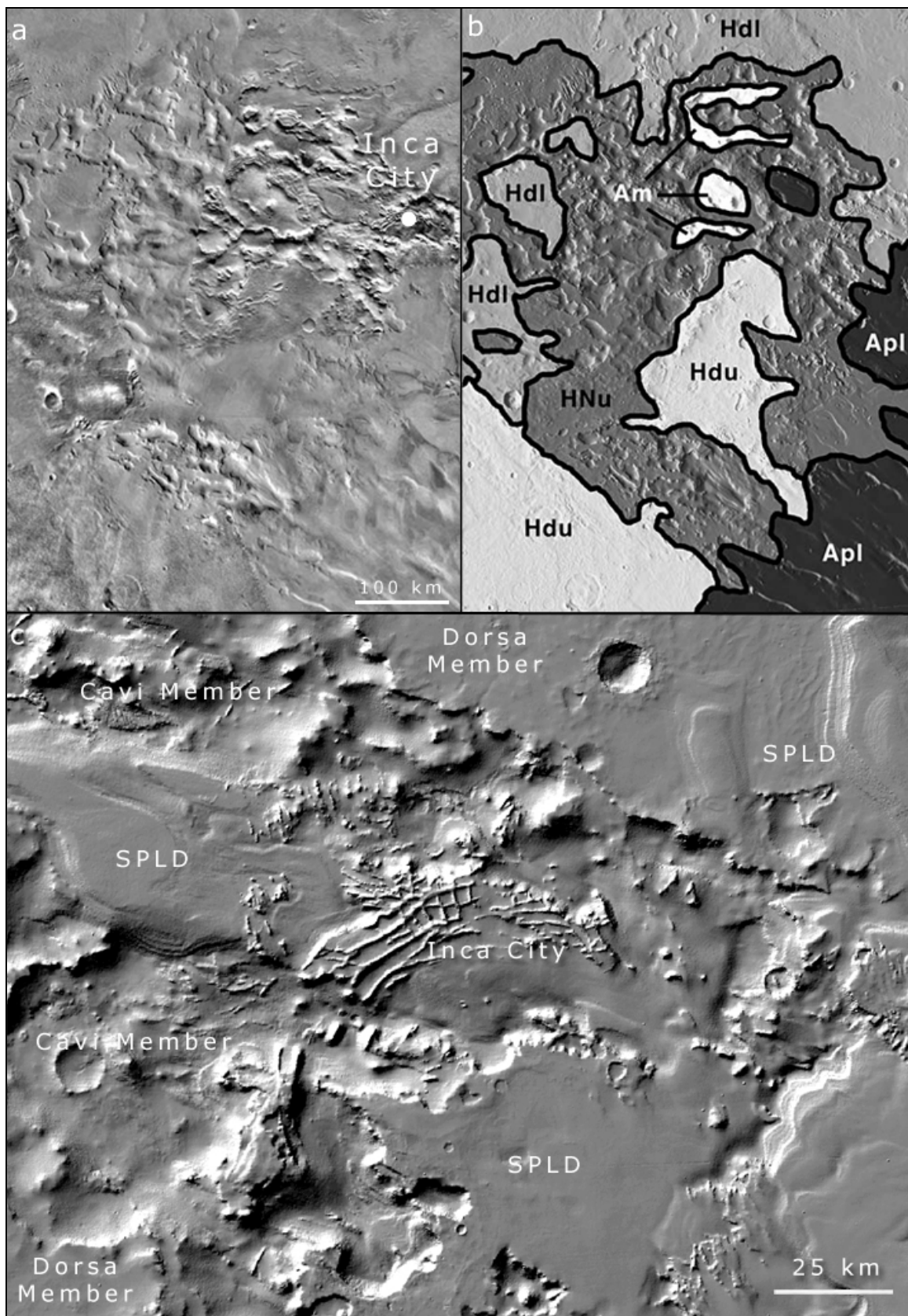


Figure 2.4. The Cavi Angusti region and the Inca City landform. **a.** Viking image mosaic of the Cavi Angusti region, redrawn after Ghatan et al. (2003). **b.** The Cavi Angusti region mapped by Tanaka and Scott (1987), redrawn after Ghatan et al. (2003). With Hdl the lower member of the DAF, Hdu the upper member of the DAF, Apl the SPLD and Am Amazonian aged mantle material. **c.** The Inca City landform mapped by Tanaka and Kolb (2001).

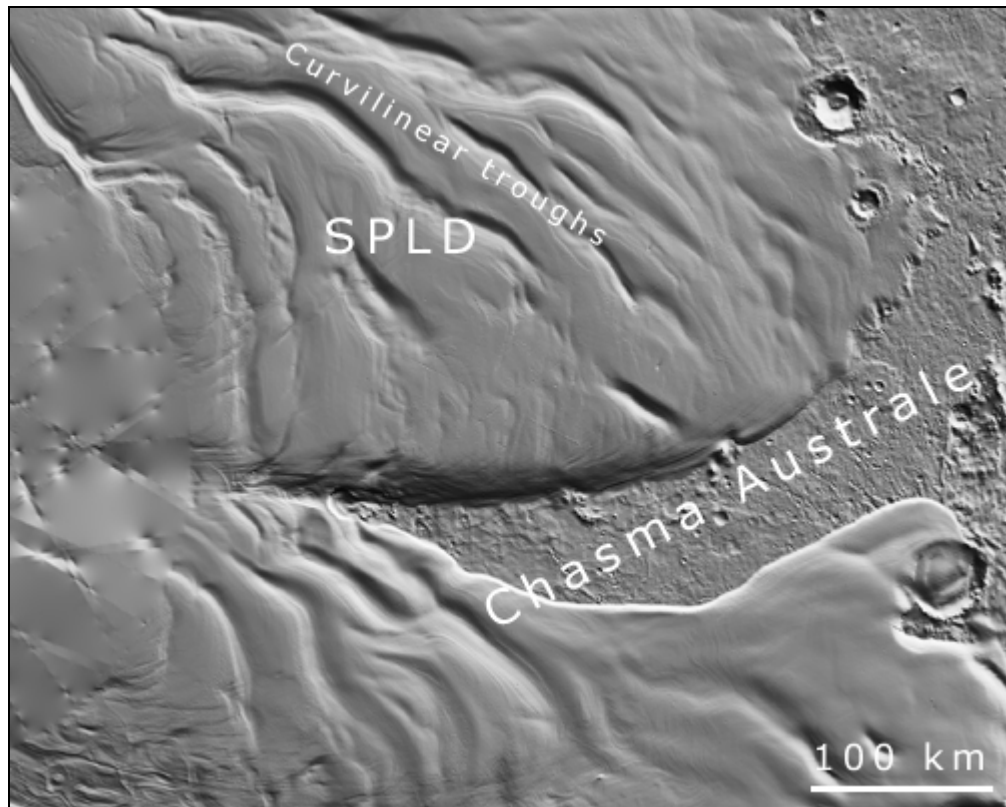


Figure 2.5. MOLA shaded relief map of Chasma Australe.

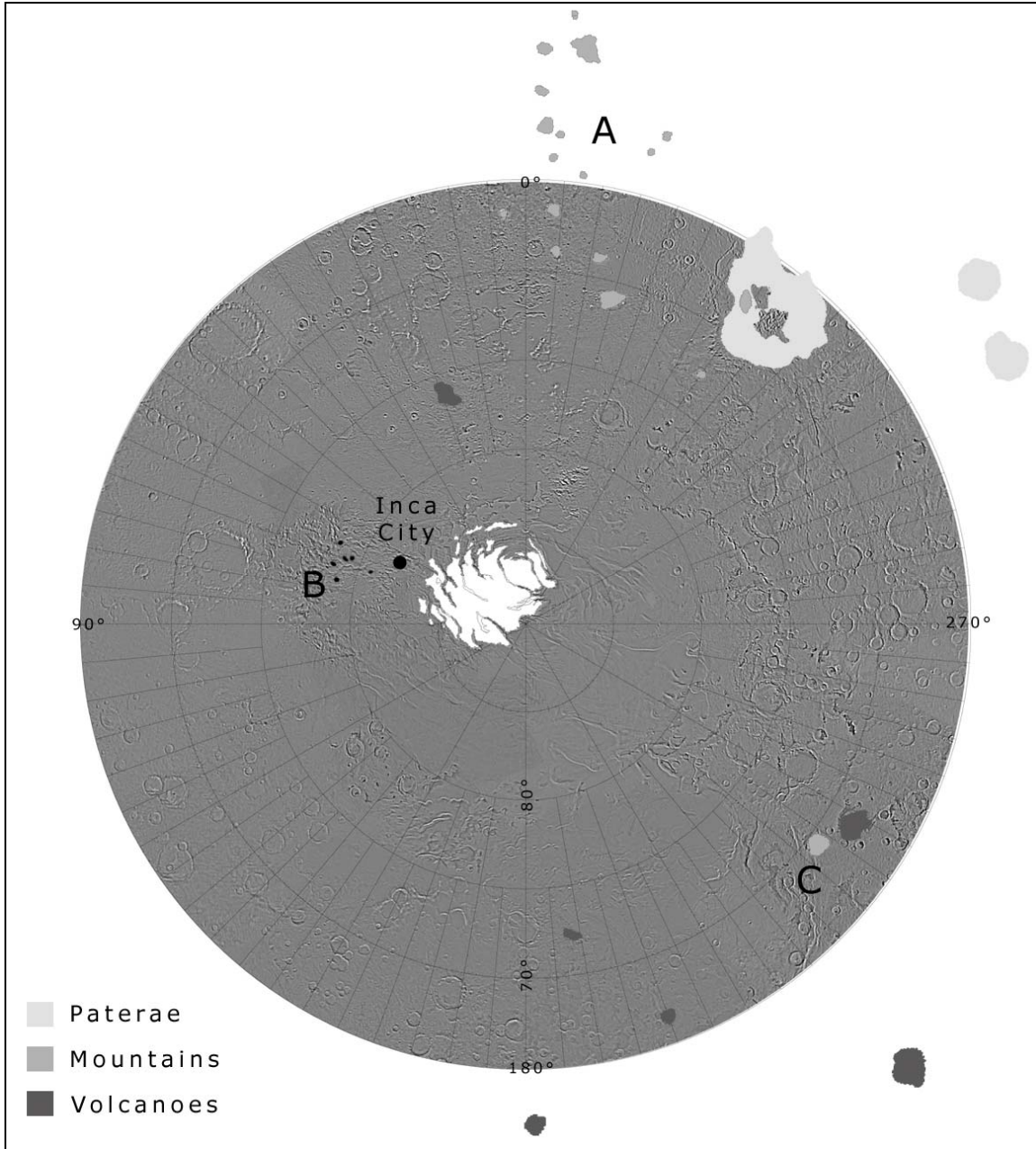


Figure 2.6. MOLA derived image of the South Polar region of Mars showing possible ancient igneous activity. A, B and C are explained in the text.

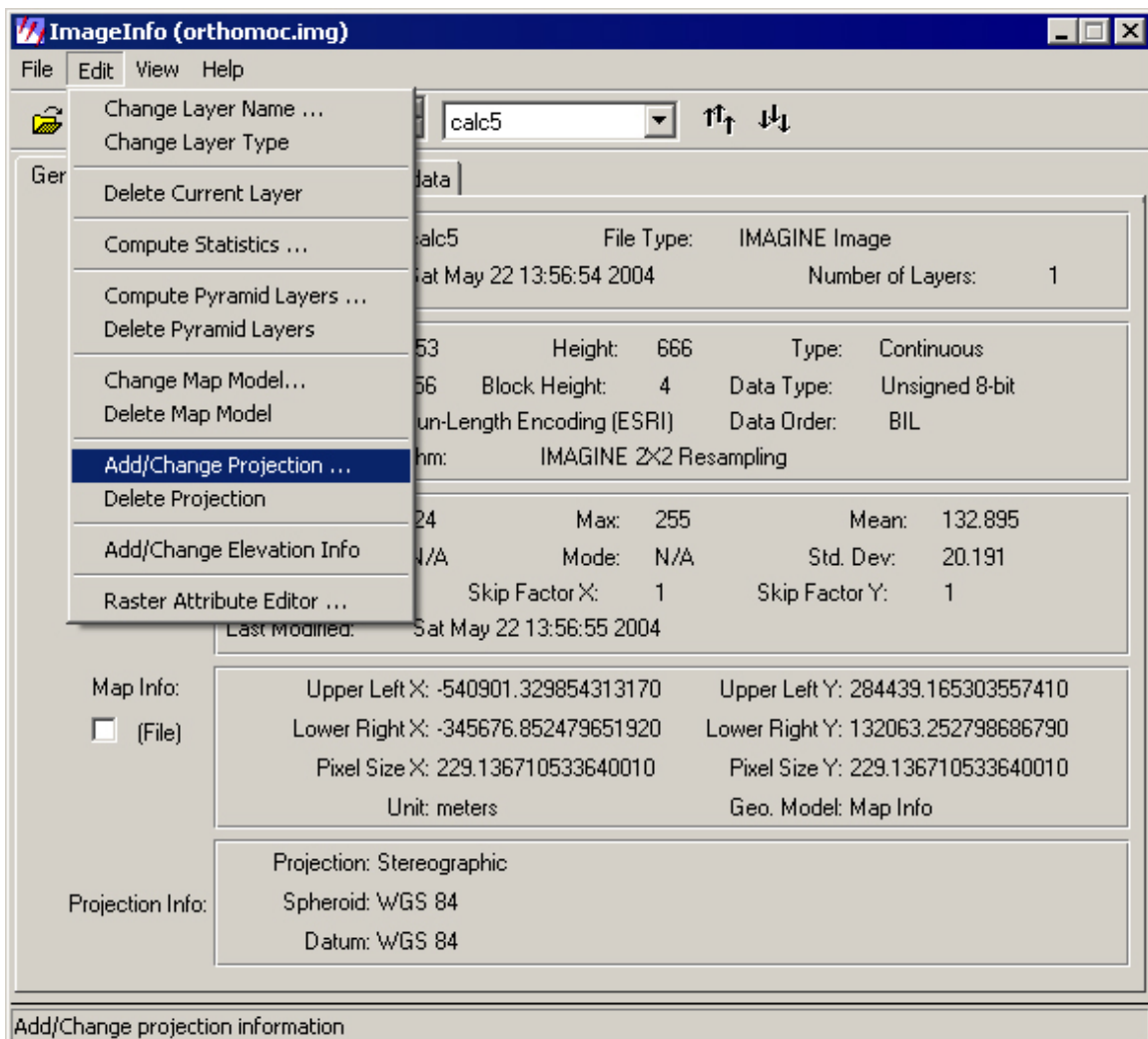


Figure 3.1. The Image Information application of ERDAS IMAGINE showing information for the horizontal reference.

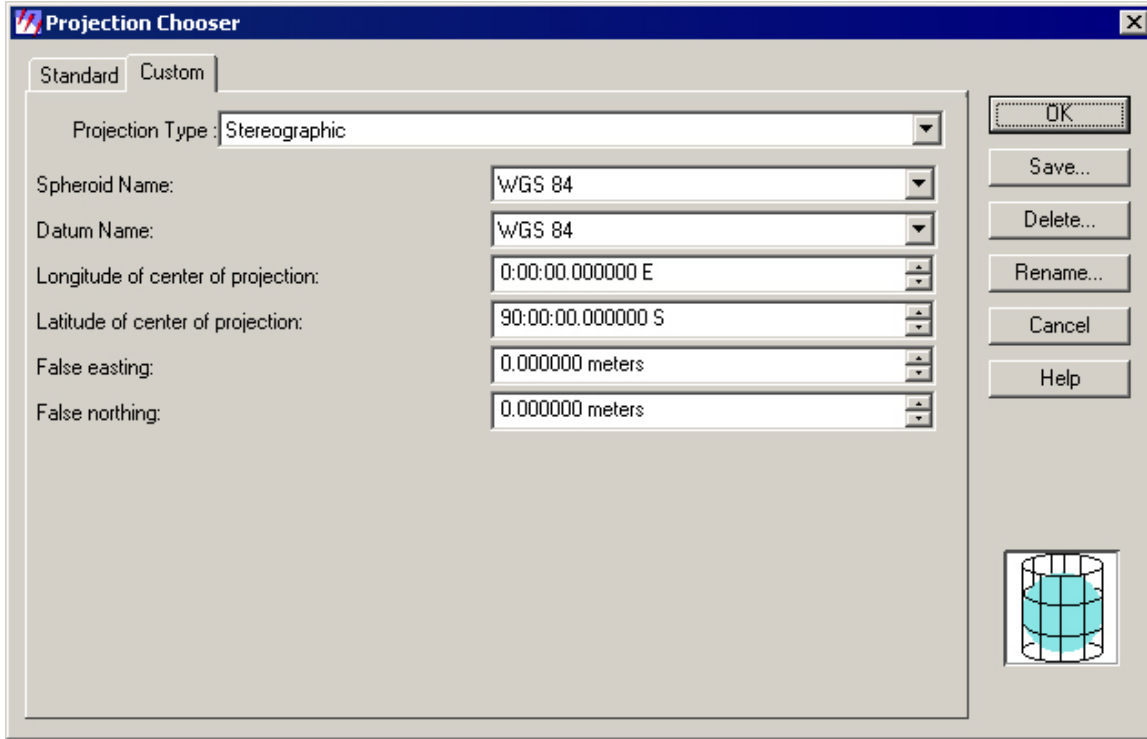


Figure 3.2. The Projection Chooser window.

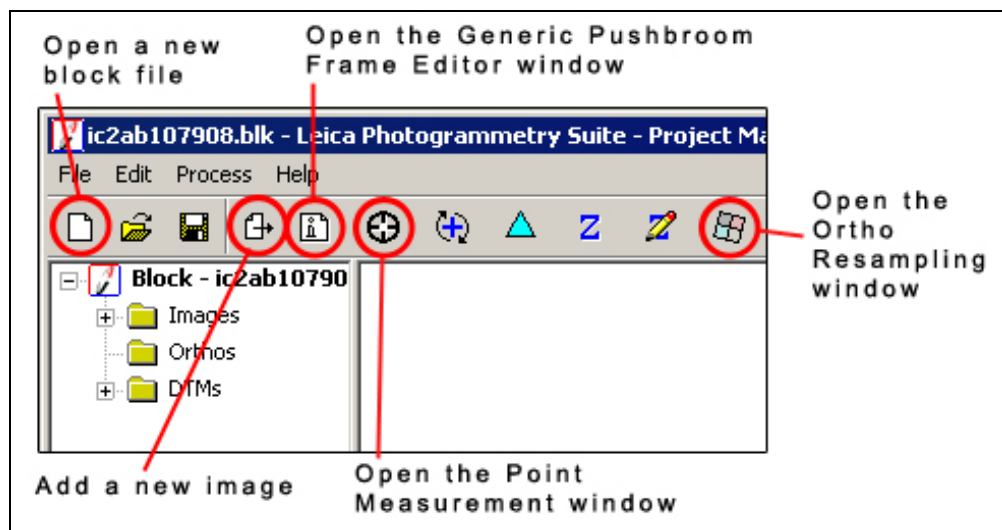


Figure 3.3. Left upper part of the Leica Photogrammetry Suite Project Manager window.

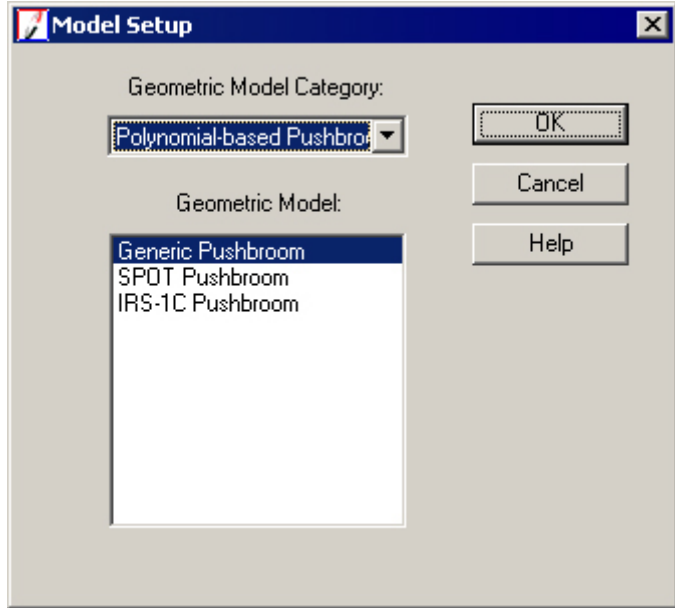


Figure 3.4. The Model Setup window.

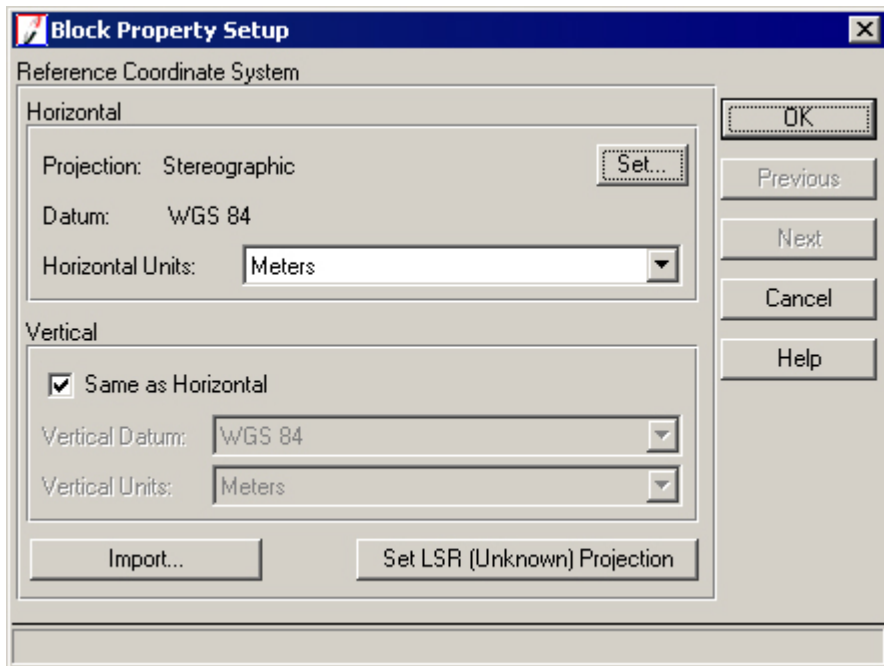


Figure 3.5. The Block Property Setup window.

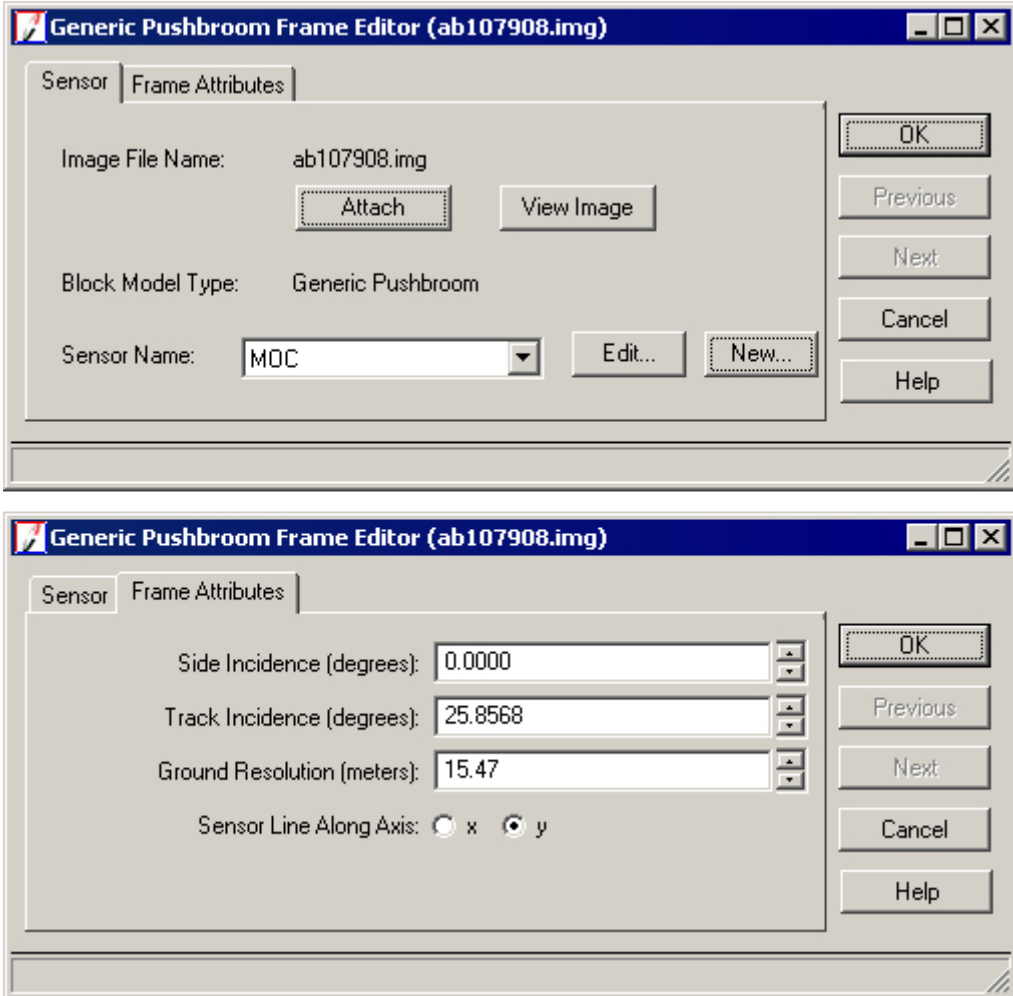


Figure 3.6. Generic Pushbroom Frame Editor window for image AB107908.

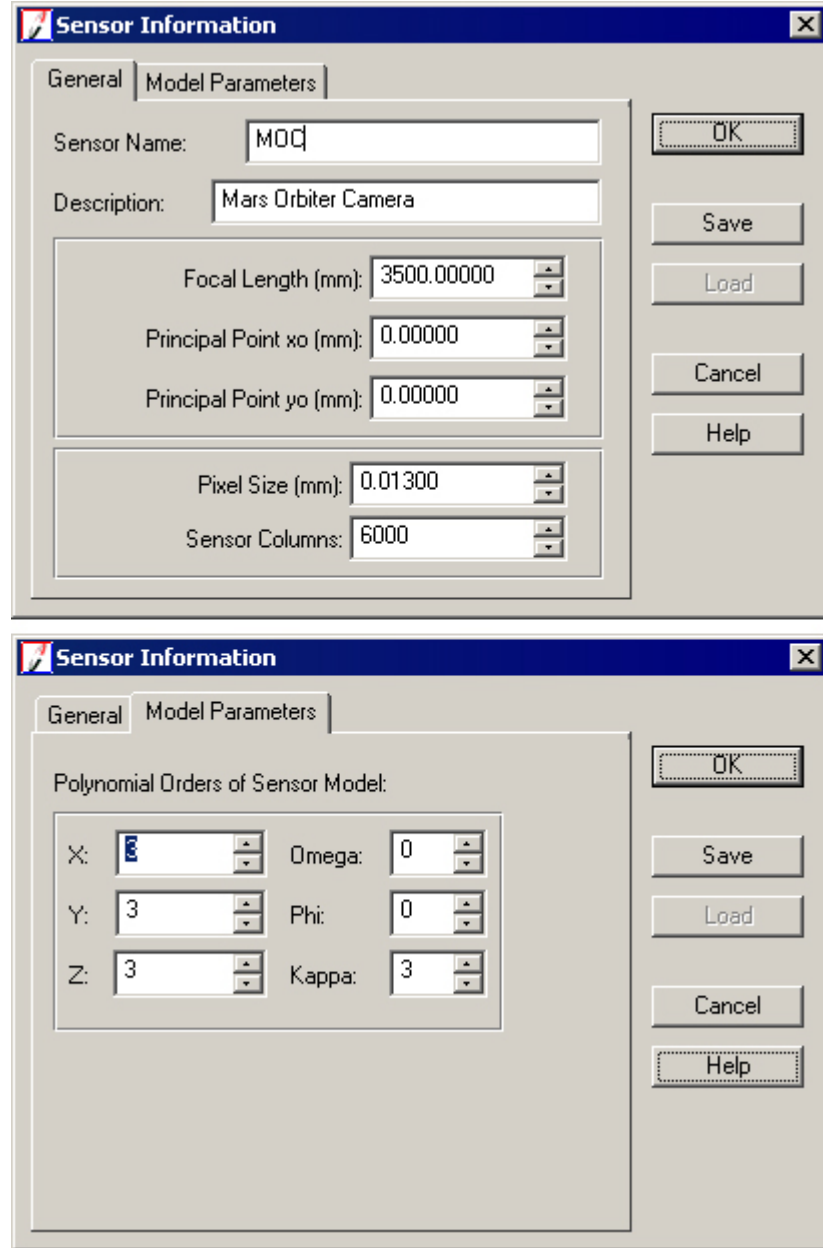


Figure 3.7. The Sensor Information window. X, Y and Z are the ground coordinate system axes. Kappa is a rotation about the photographic z-axis. The standard order for X, Y, Z and Kappa is 2 but by trial-and-error a 3rd order transformation was assigned. The Omega and Phi are standard, and set to zero.

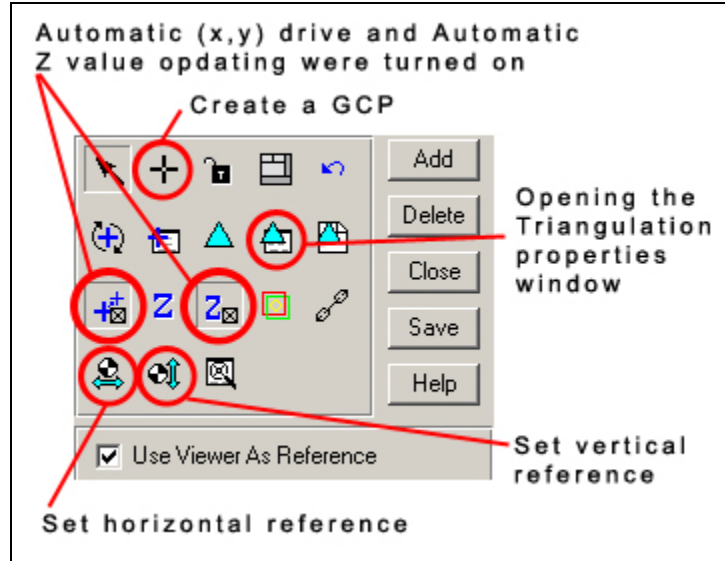


Figure 3.8. Options in the upper right corner of the Point Measurement window. The ‘Automatic (x,y) drive’ automatically displays the image position of GCPs in the right and left viewers of the Point Measurement window. ‘Automatic Z value updating’ automatically updates the Z values when a new point is created in the GCP table of the Point Measurement window.

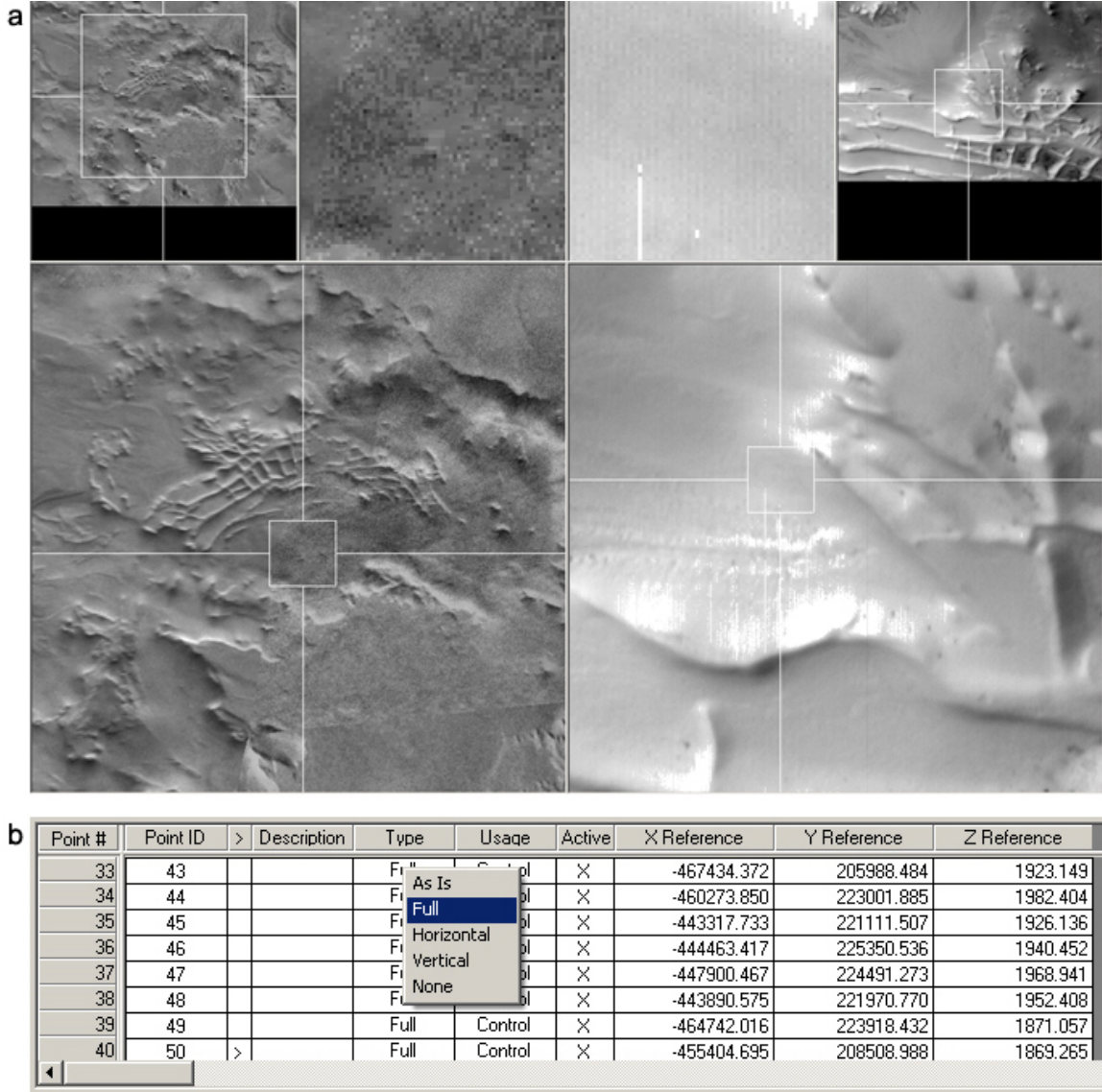


Figure 3.9. **a.** The left and right viewers in the Point Measurement window. The left viewer shows the horizontal reference and the right viewer shows image AB1-07908. **b.** The GCP Table in the lower left of the Point Measurement window.

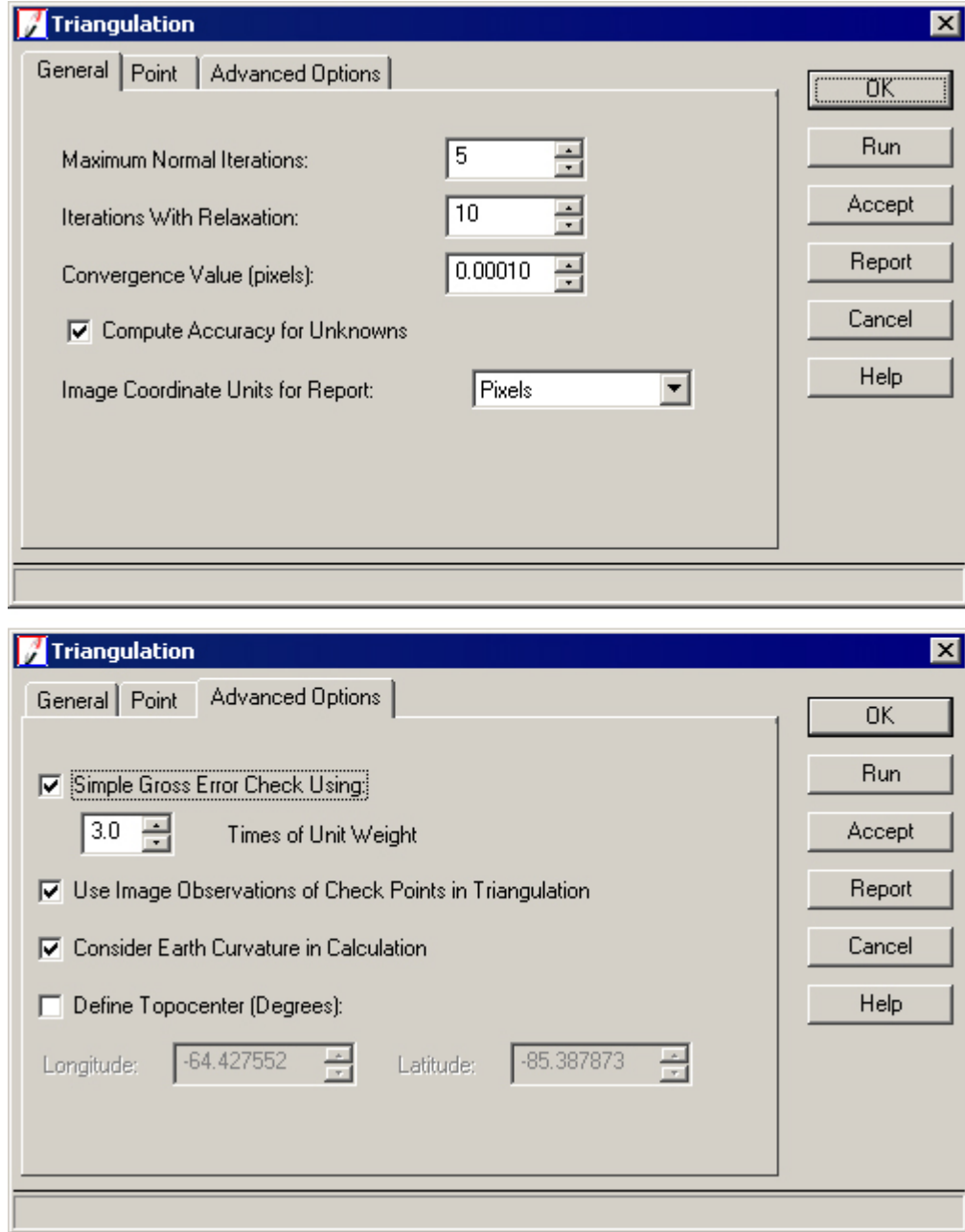


Figure 3.10. The Triangulation properties window.

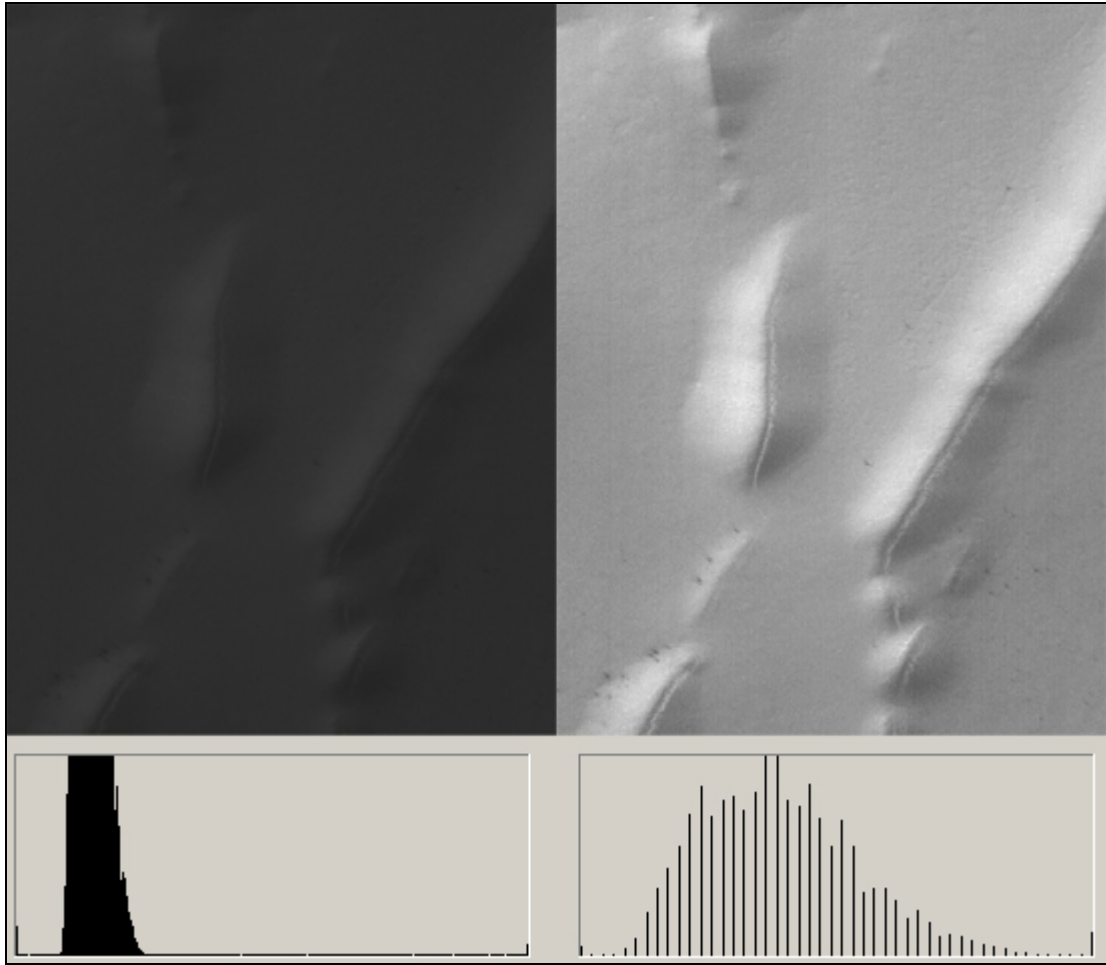


Figure 3.11. Effects of a contrast enhancement procedure on MOC NA image E0500171 using the ‘level adjustment’ tool from Adobe Photoshop. The left image is unprocessed and the right image is processed. Below the images, the respective histograms are shown.

Acquisition parameters		Derived values	
<u>Image ID (picno)</u> :	E04-01193	<u>Longitude of image center</u> :	63.78°W
<u>Image start time</u> :	2001-05-17T02:50:32.51 SCET	<u>Latitude of image center</u> :	81.57°S
<u>Image width</u> :	256 pixels	<u>Scaled pixel width</u> :	11.03 meters
<u>Image height</u> :	1536 pixels	<u>Scaled image width</u> :	2.83 km
<u>Line integration time</u> :	0.7231 millisec	<u>Scaled image height</u> :	27.10 km
<u>Pixel aspect ratio</u> :	1.59	<u>Solar longitude (Ls)</u> :	162.60°
<u>Crosstrack summing</u> :	8	<u>Local True Solar Time</u> :	15.98 decimal hours
<u>Downtrack summing</u> :	8	<u>Emission angle</u> :	0.17°
<u>Compression type</u> :	MOC-PRED-X-5	<u>Incidence angle</u> :	93.03°
<u>Gain mode</u> :	0A (hexadecimal)	<u>Phase angle</u> :	92.89°
<u>Offset mode</u> :	4 (decimal)	<u>North azimuth</u> :	110.61°
		<u>Sun azimuth</u> :	51.40°
		<u>Spacecraft altitude</u> :	371.30 km
		<u>Slant distance</u> :	371.30 km

Figure 3.12. Ancillary data obtained from the download page of image E04-01193 in the MOC Gallery.

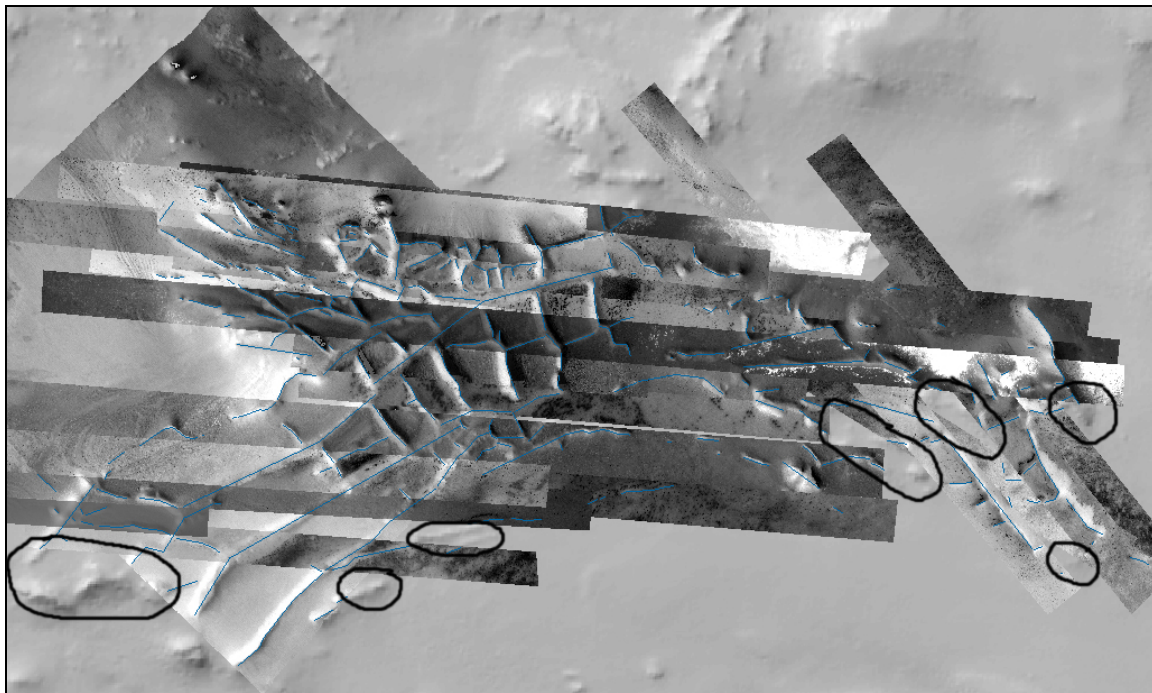


Figure 3.13. The MOC NA mosaic and a shaded relief map, made from the ~114 m/p MOLA DEM, in the background. The black circles show the parts of Inca City, which are not covered by the mosaic.

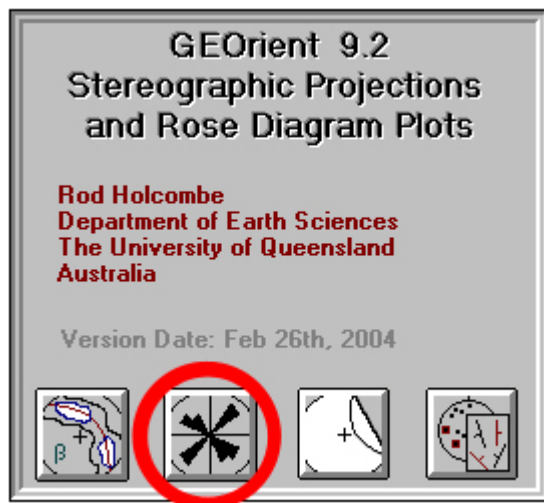


Figure 3.14. The introduction menu of GEOrient. The button inside the red circle opens the Rose Diagram section.

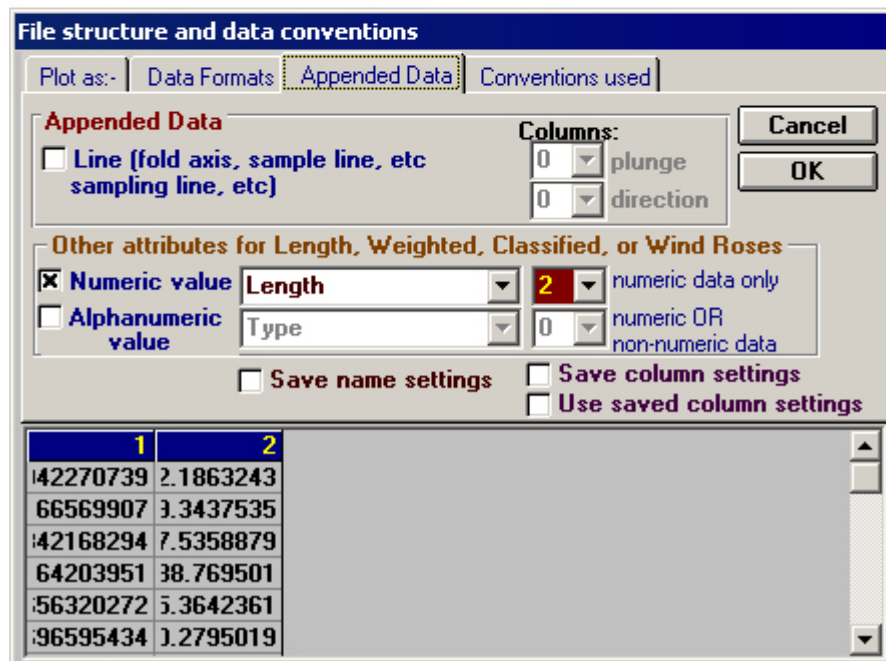
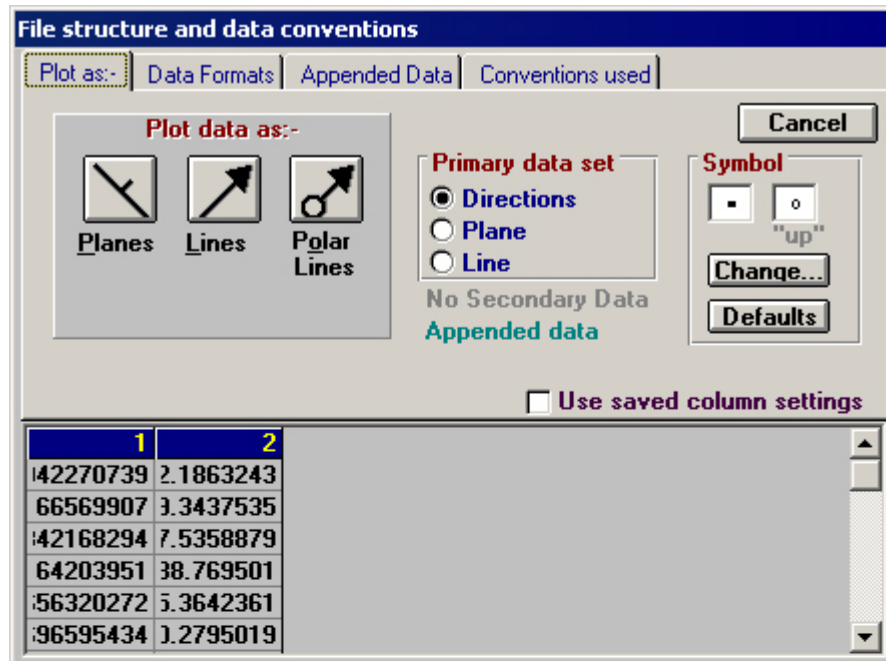


Figure 3.15. The ‘File structure and data conventions’ window.

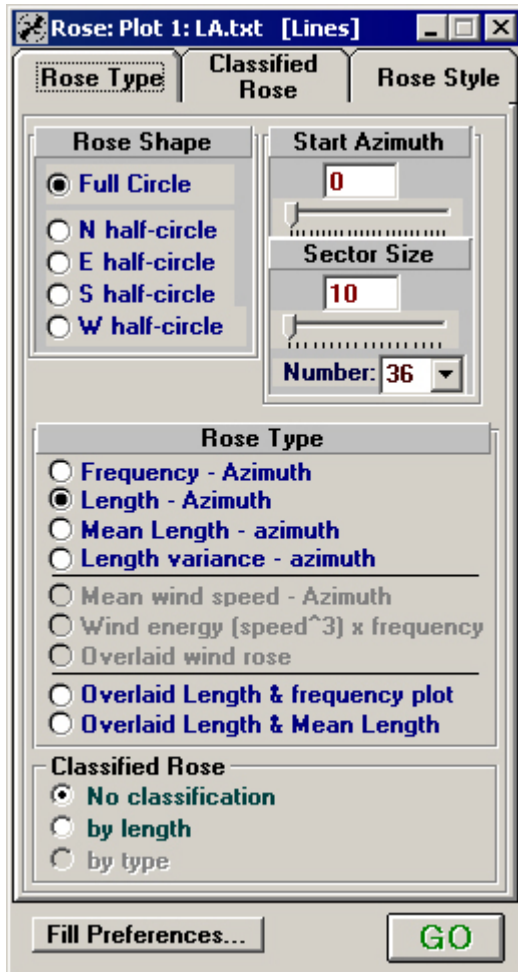


Figure 3.16. The Rose: Plot window.

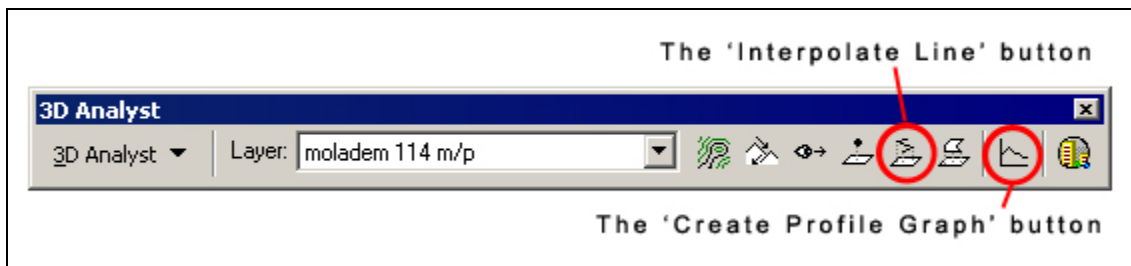


Figure 3.17. The '3D Analyst' tool of ArcMap.

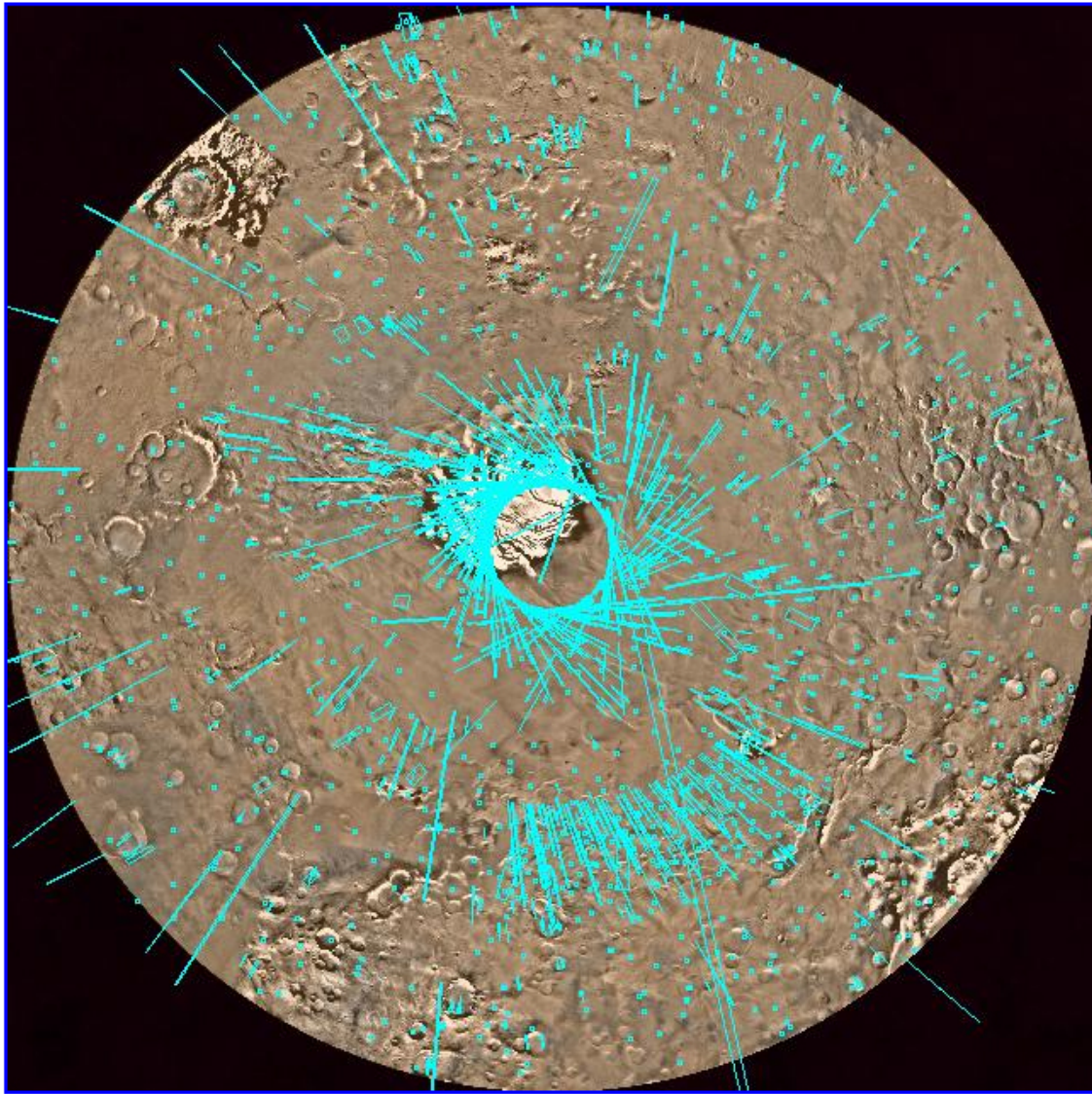


Figure 3.18. Example of a map of the South Polar Region of Mars including the footprints of the MOC NA images, taken from the MSSS MOC Gallery. The images displayed here were taken between September 1997 and August 1999 (Mission Subphases AB1 through M04).

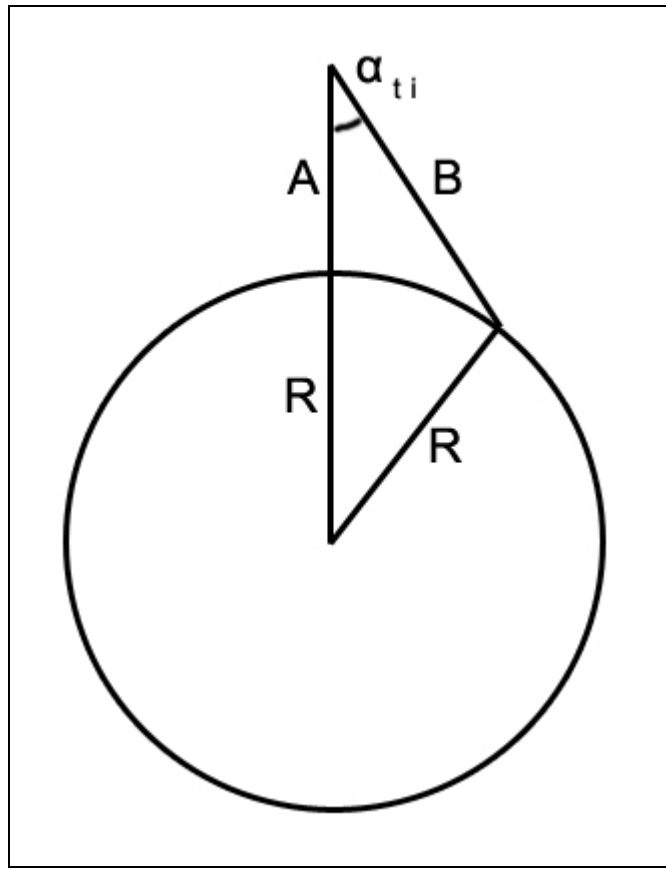


Figure 3.19. For an explanation see Appendix II.

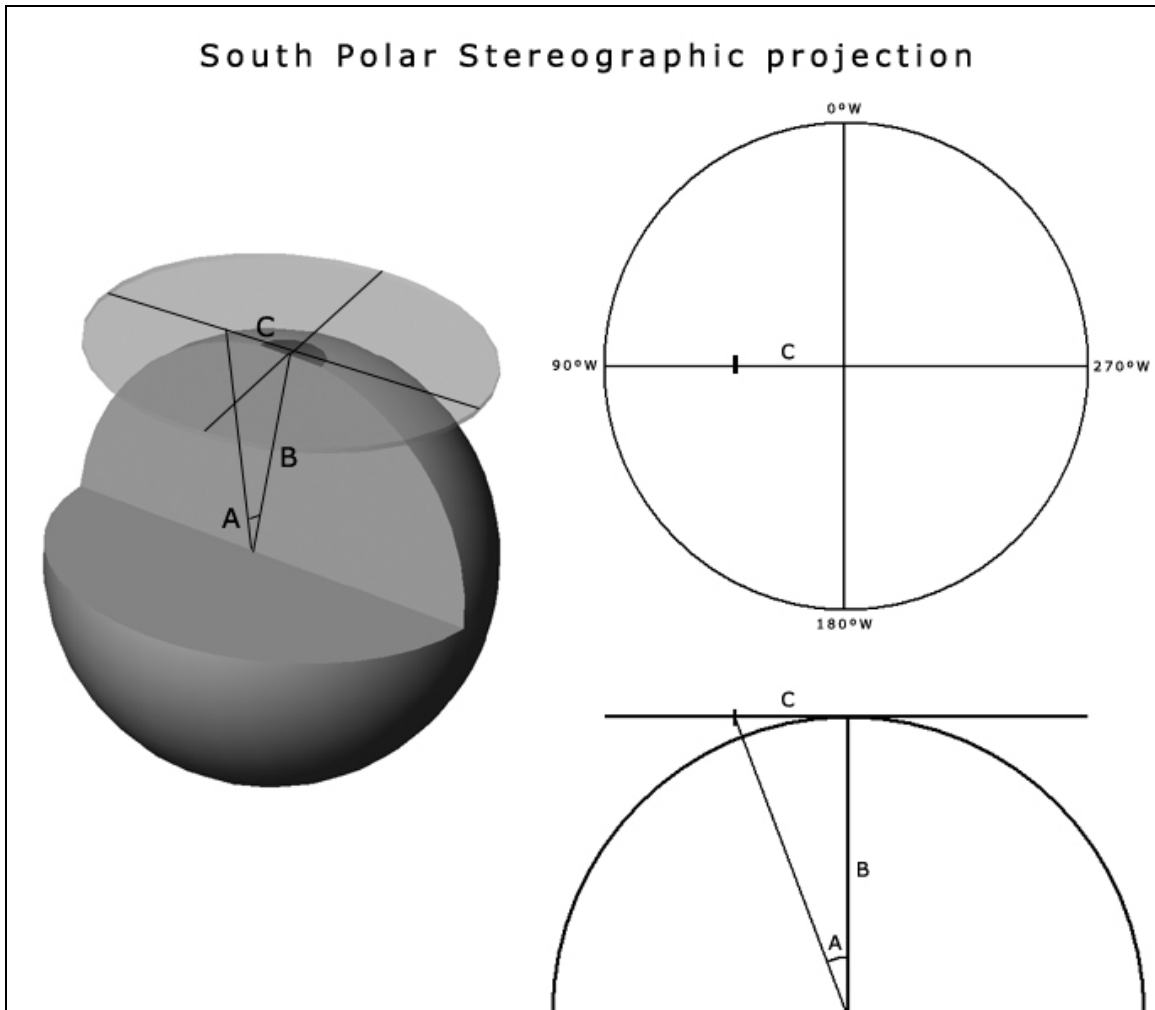


Figure 3.20. For an explanation see Appendix III.

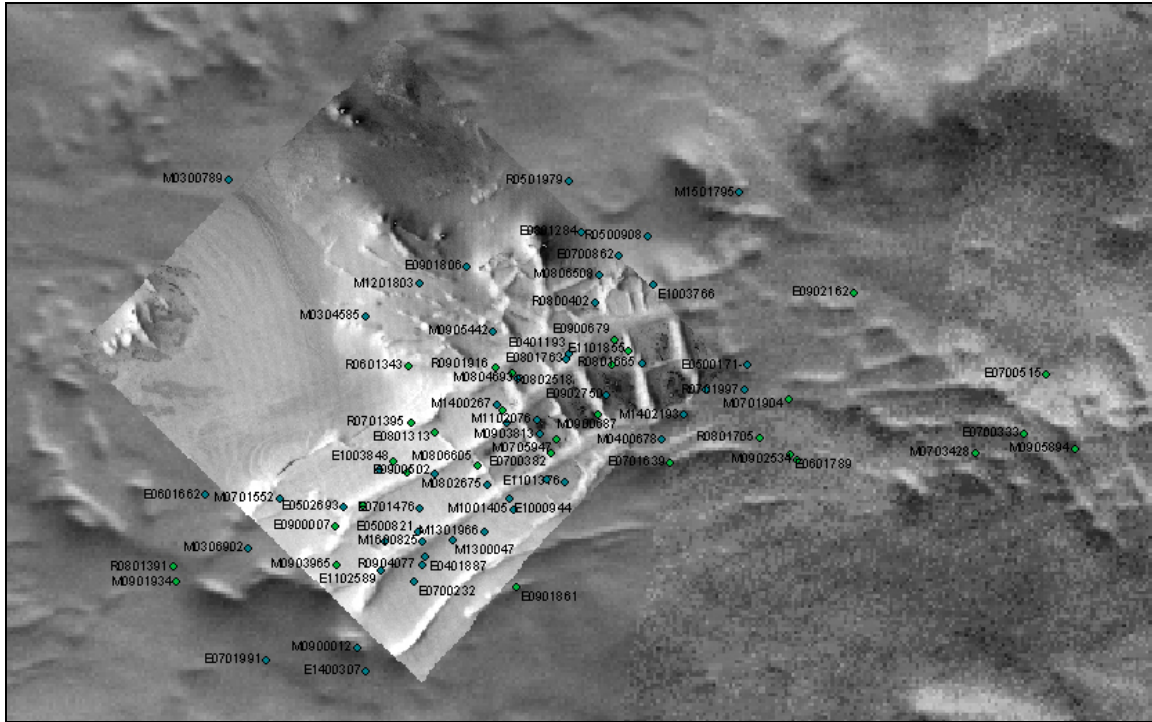


Figure 3.21. Part of an ArcMap window showing the names and the locations of the image center of all the 87 MOC NA slices, projected on Inca City (orthoimage AB1-07908 and the horizontal reference).

Figure 4.1. MOC NA mosaic.

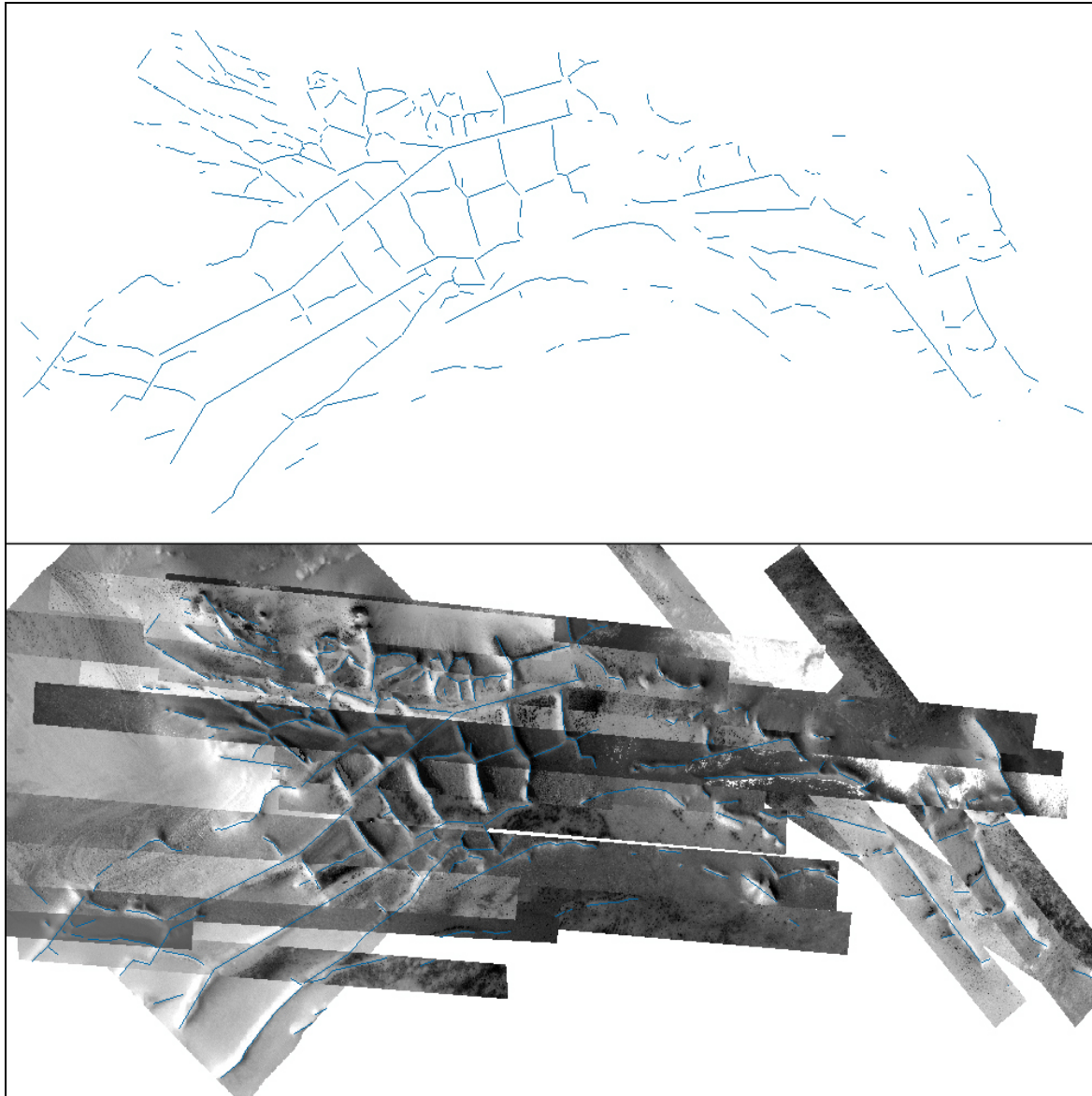


Figure 4.2. Lineaments of Inca City created on top of the mosaic of MOC NA images with the ArcMap Editor.

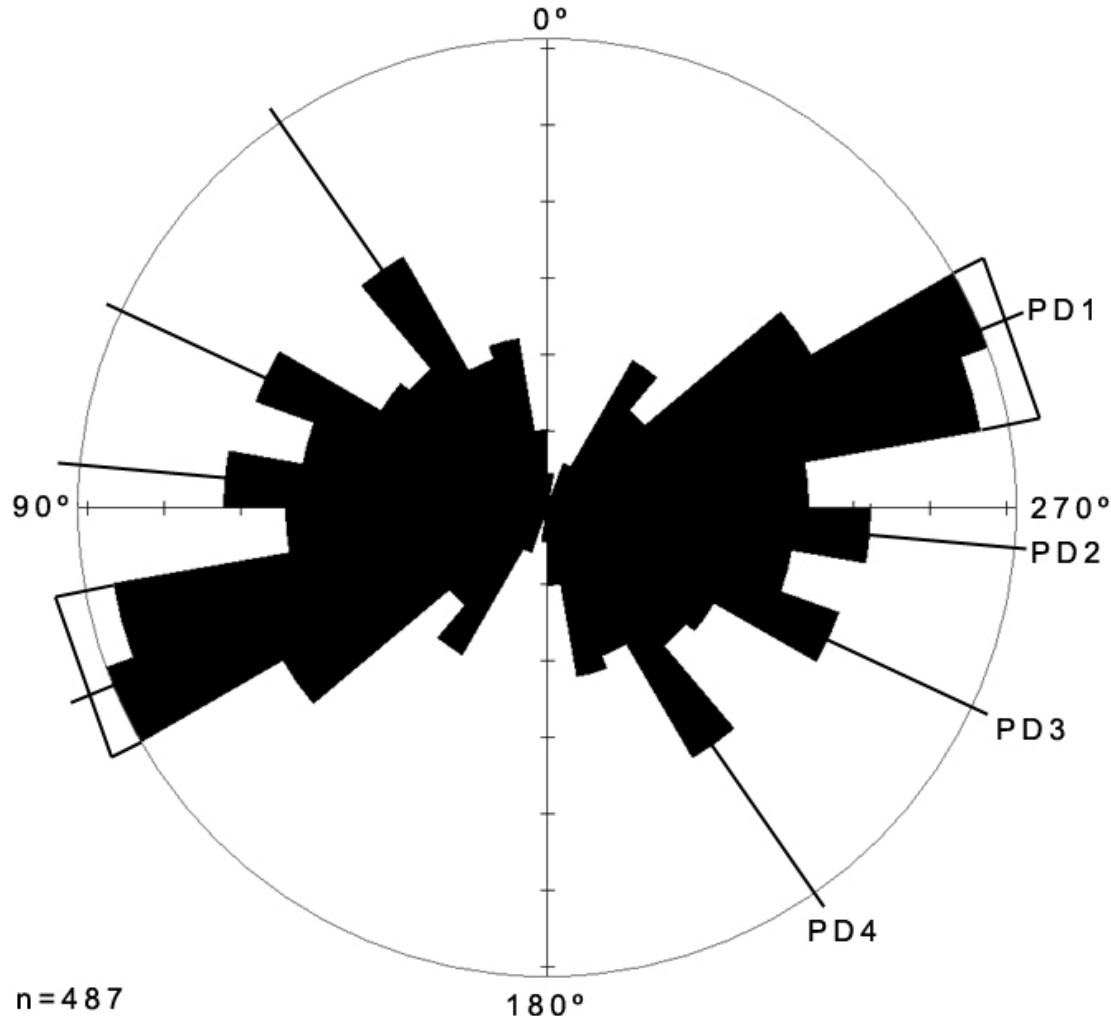


Figure 4.3. Length-weighted Rose Diagram of the Inca City ridges. The total length of all the lineaments is 479908.1 m and the largest lineament is 12.3% (58868.8 m) of the total length.

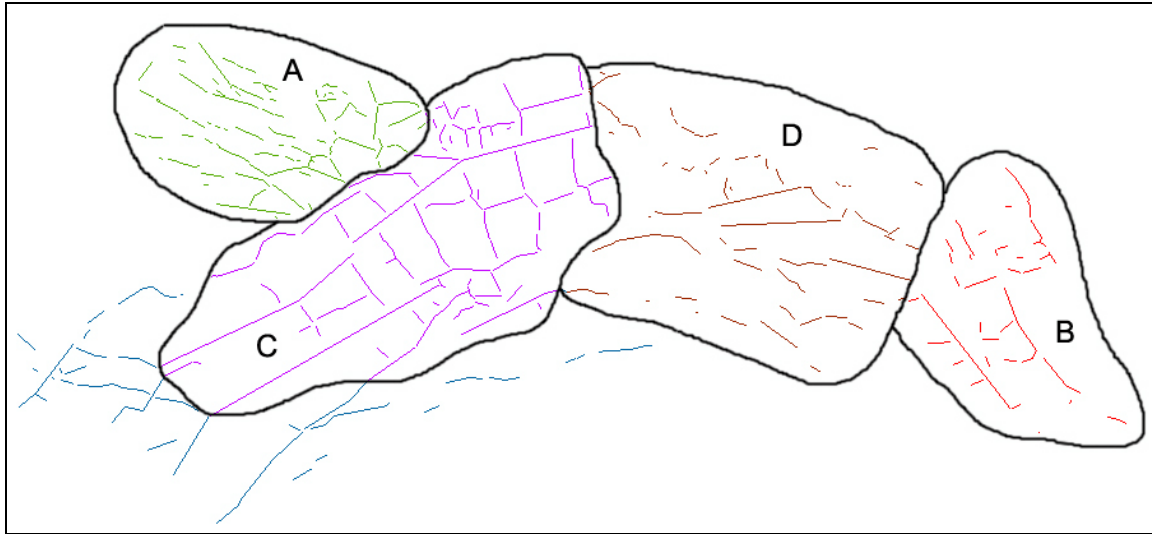


Figure 4.4. Four different domains were defined.

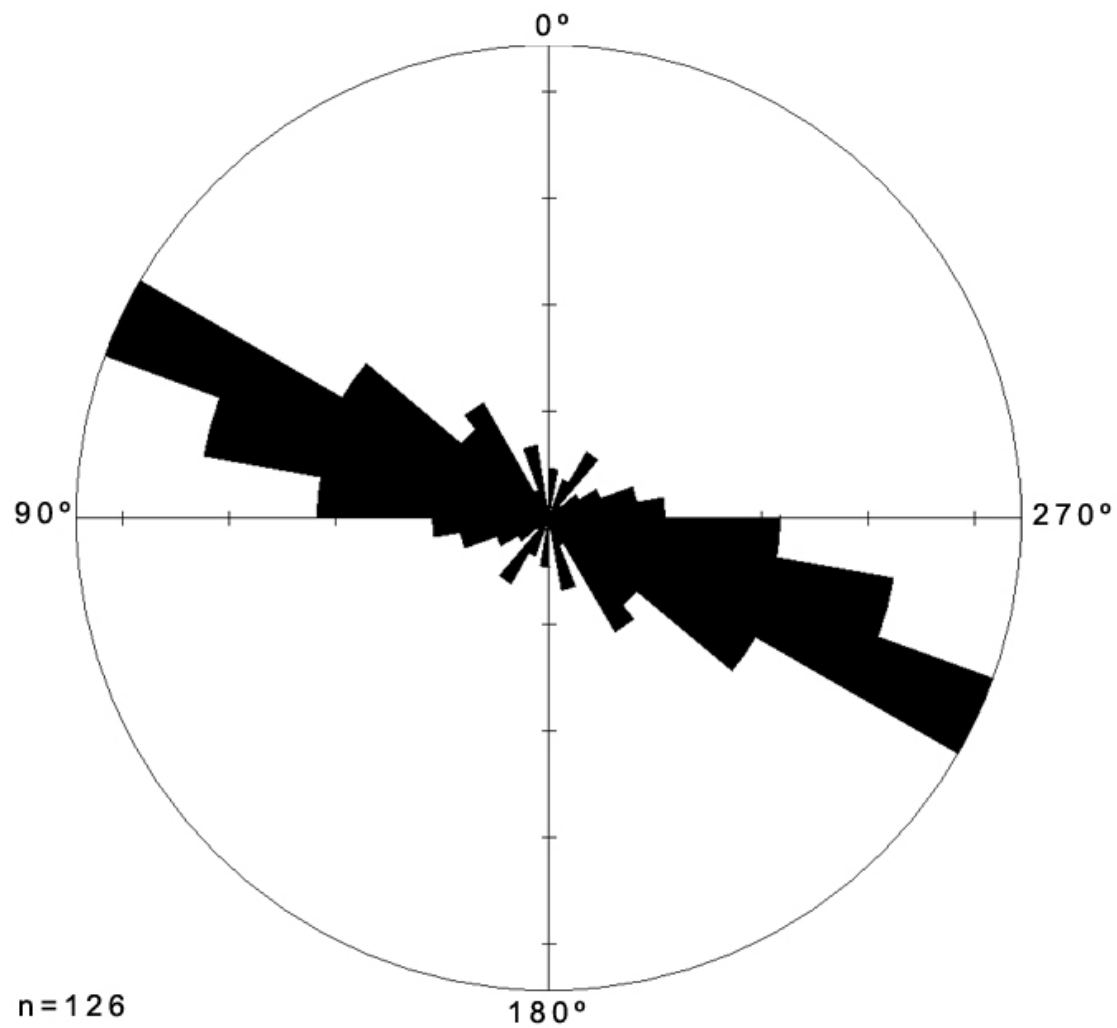


Figure 4.5. Length-weighted Rose Diagram of Domain A.

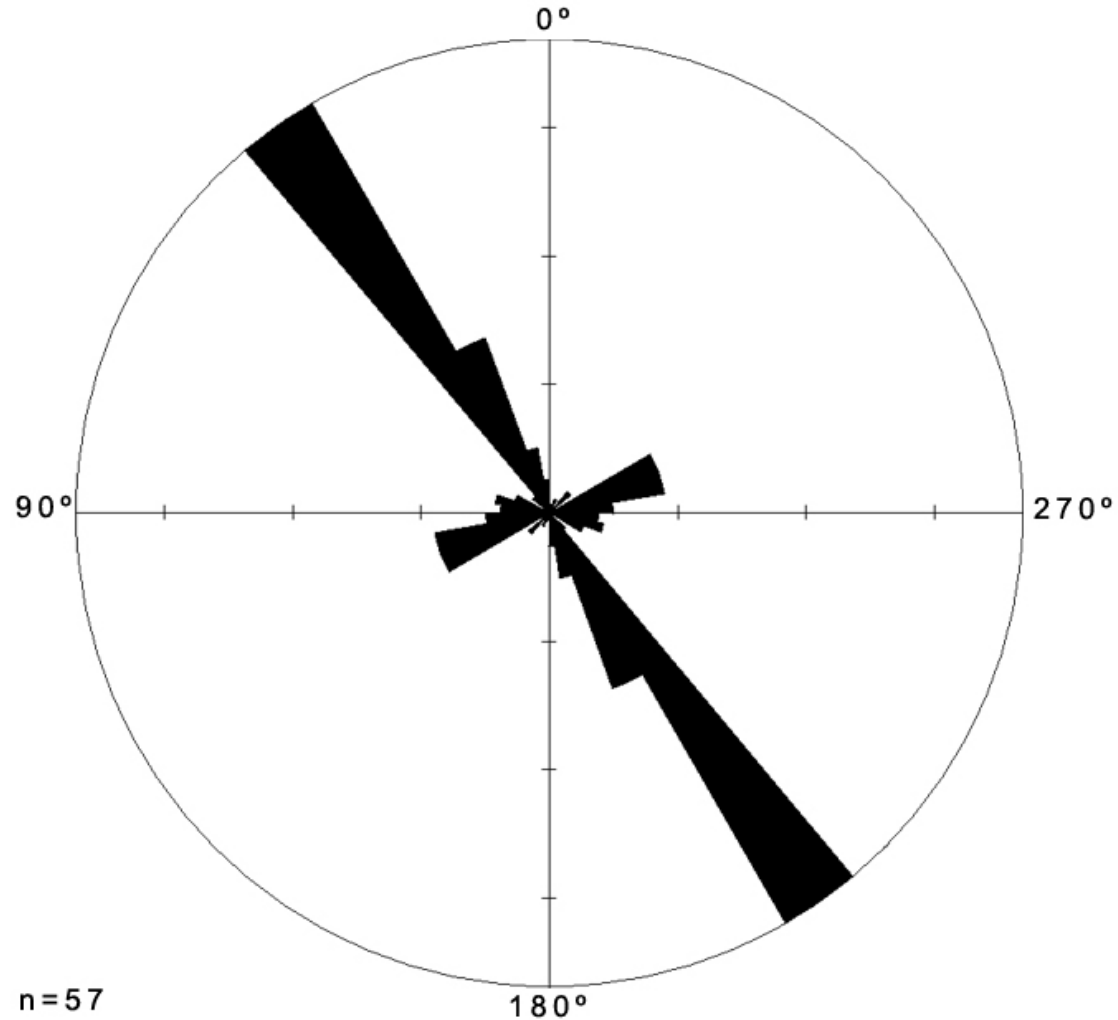


Figure 4.6. Length-weighted Rose Diagram of Domain B.

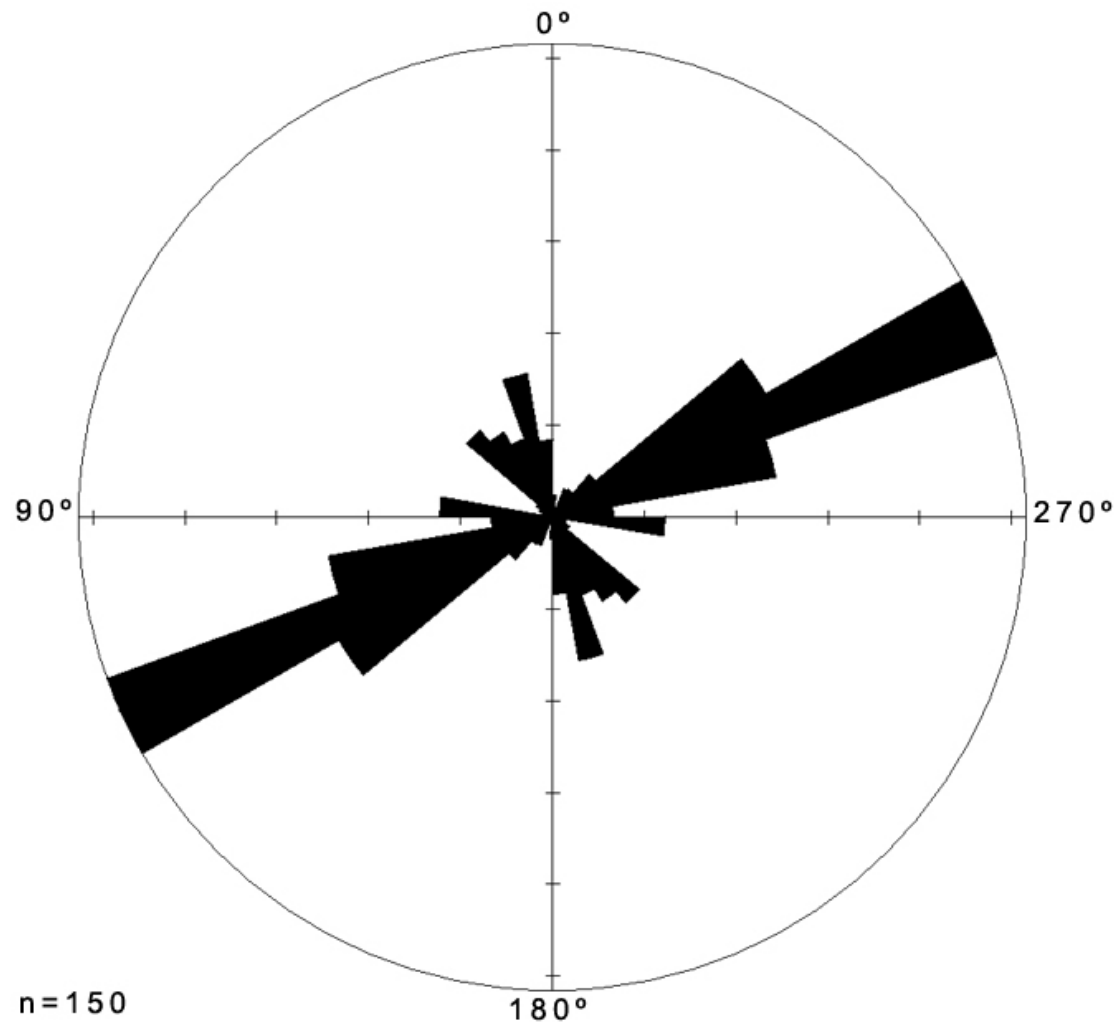


Figure 4.7. Length-weighted Rose Diagram of Domain C.

70

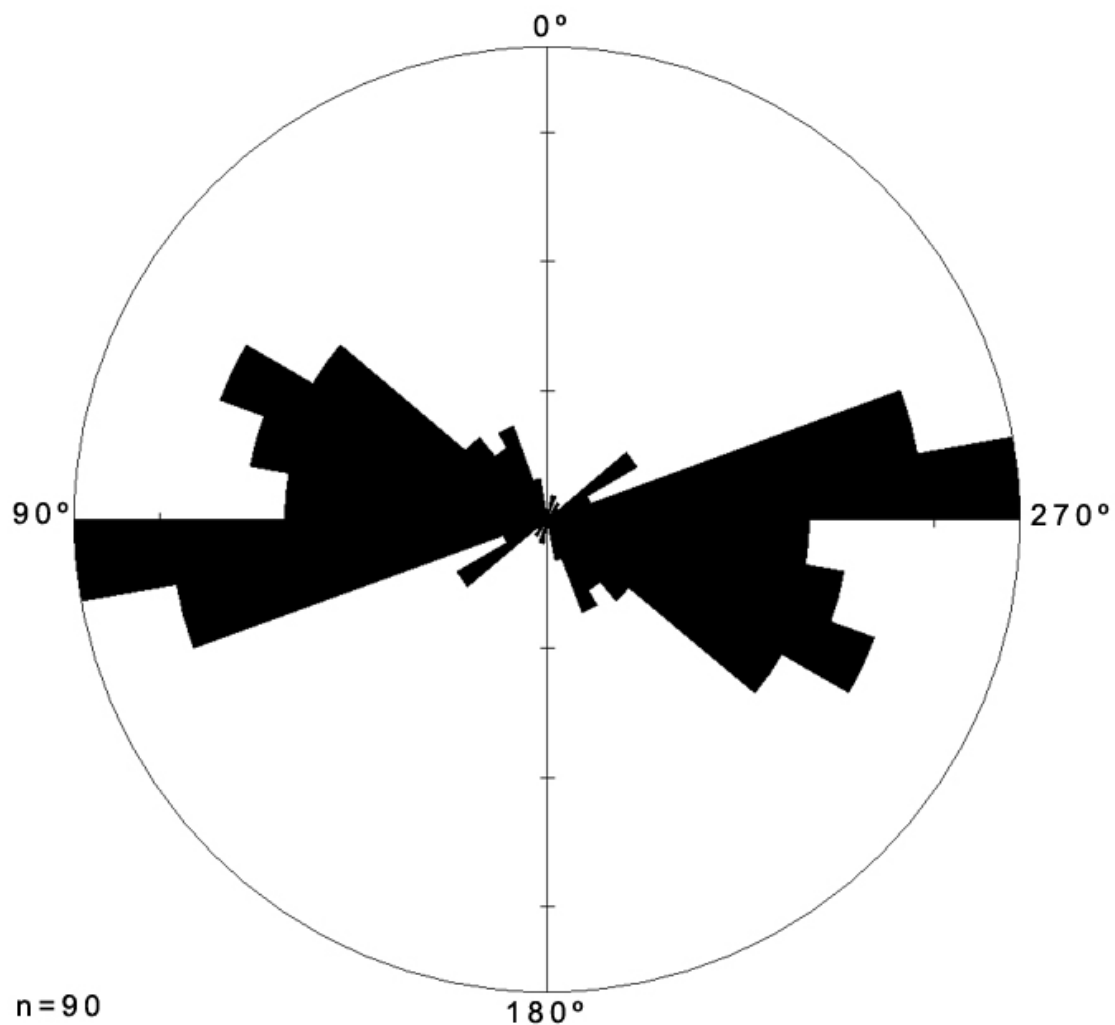


Figure 4.8. Length-weighted Rose Diagram of Domain D.

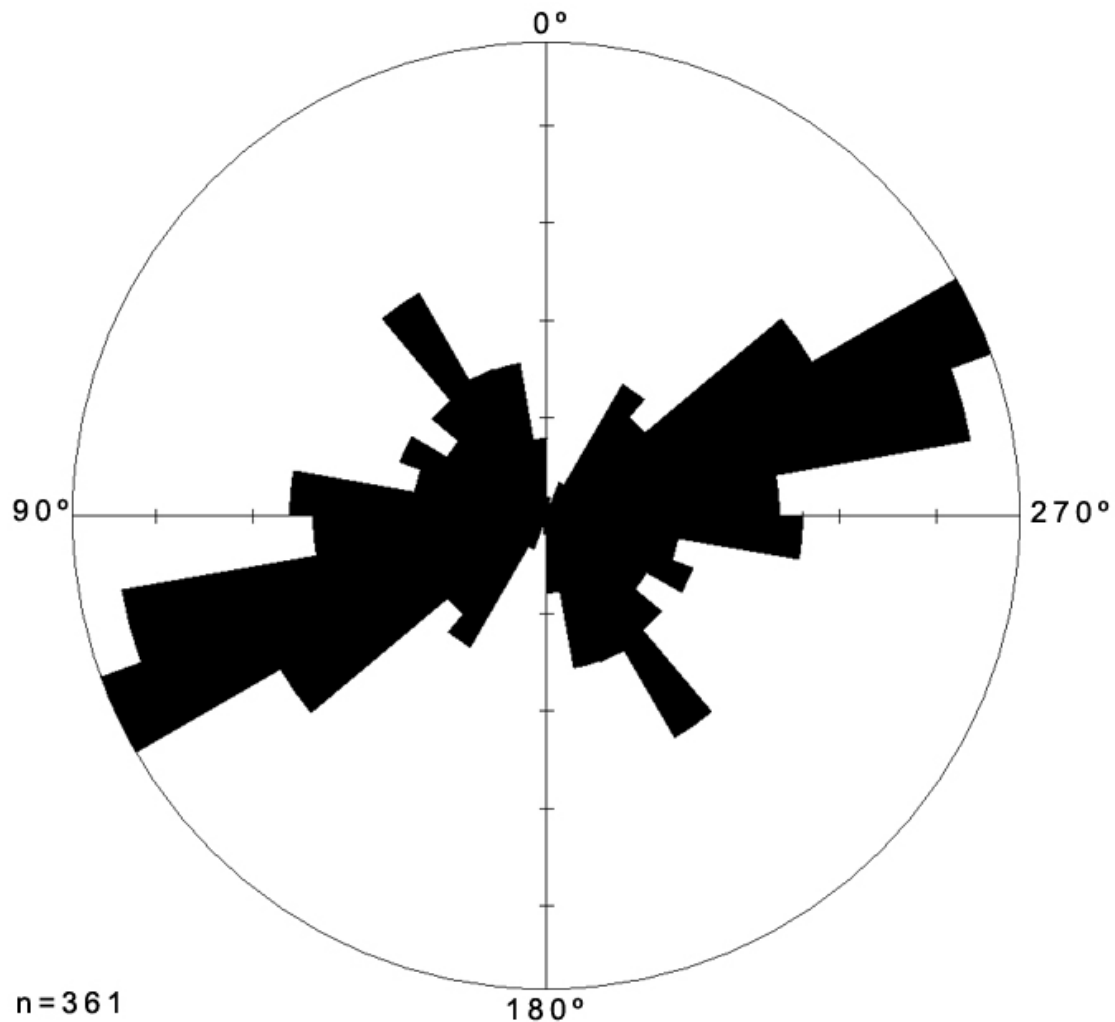


Figure 4.9. Length-weighted Rose Diagram of all lineaments of Inca City except Domain A.

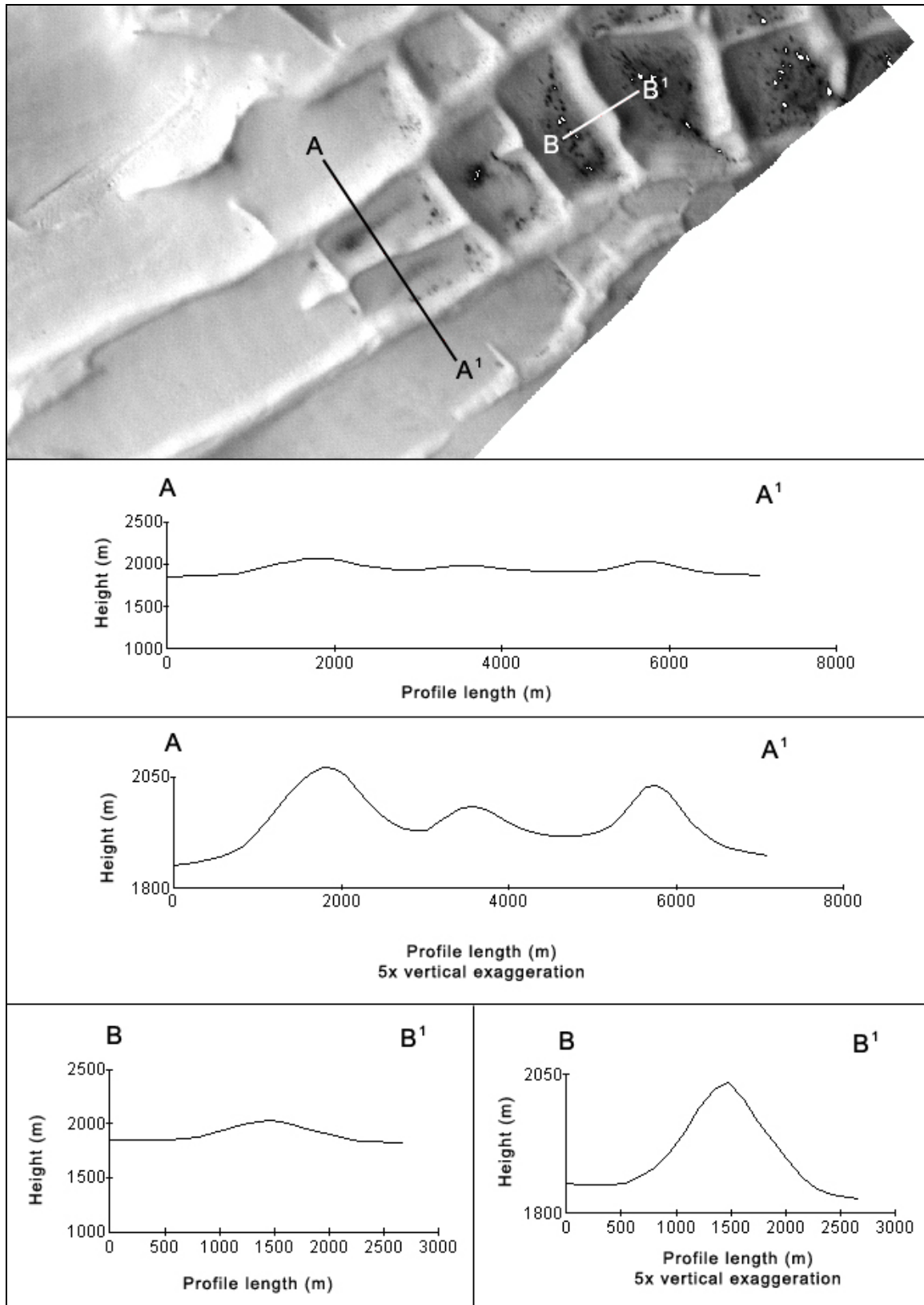


Figure 4.10. Profiles of Inca City ridges using the ~114 m/p MOLA DEM.

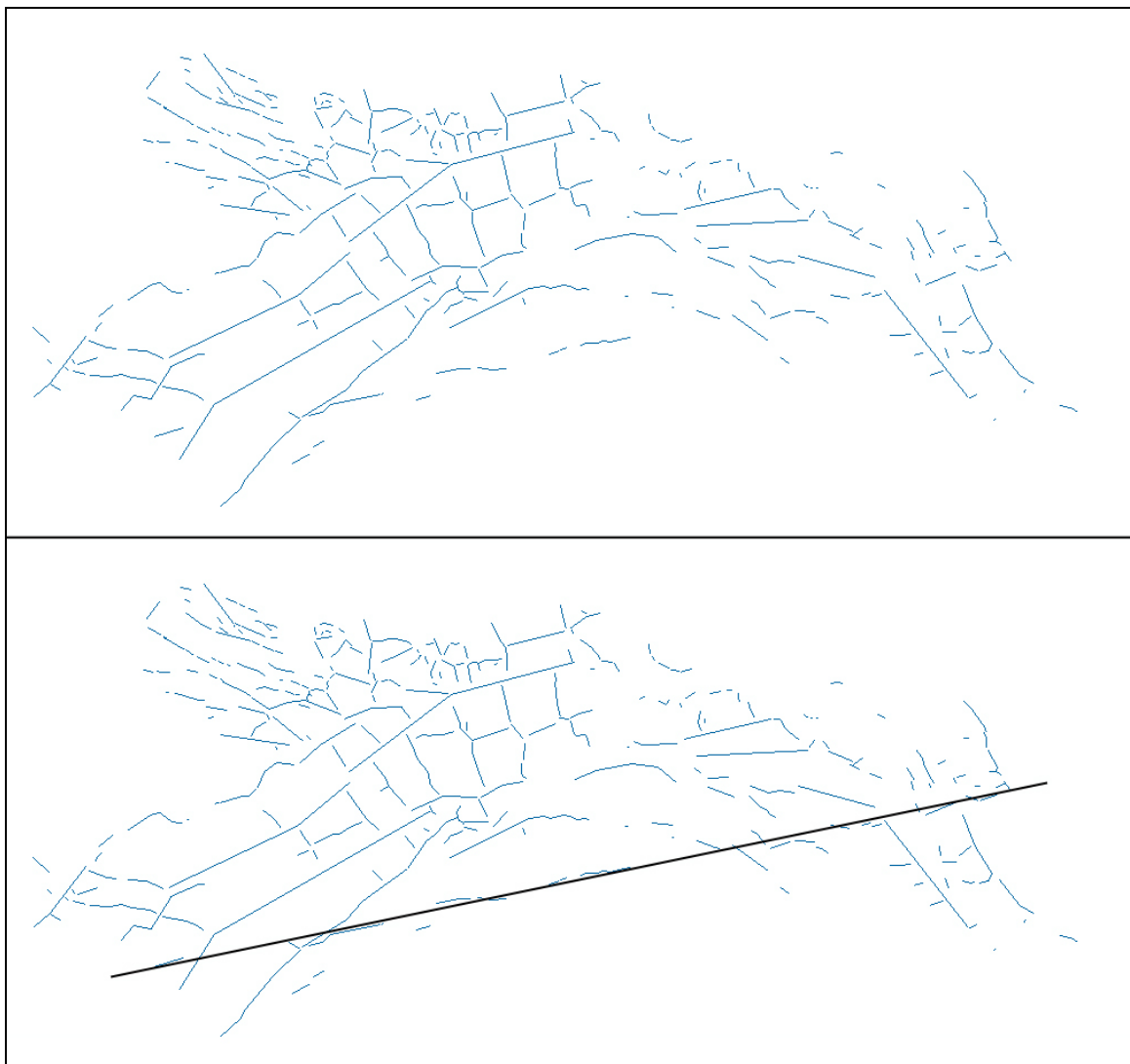


Figure 4.11. A linear trend observed in the Inca City lineaments.

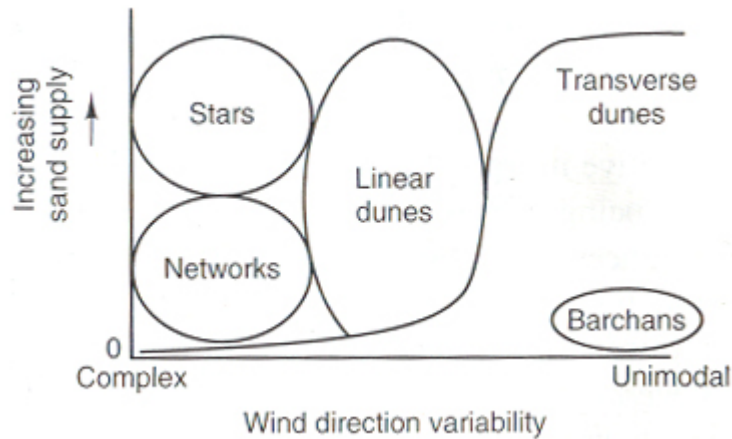


Figure 5.1. A speculative model describing the relationship between wind direction variability and sand supply in controlling dune types. Network dunes are a specific type of star dunes and barchans are a specific type of transverse dunes. After Livingstone and Warren (1996).

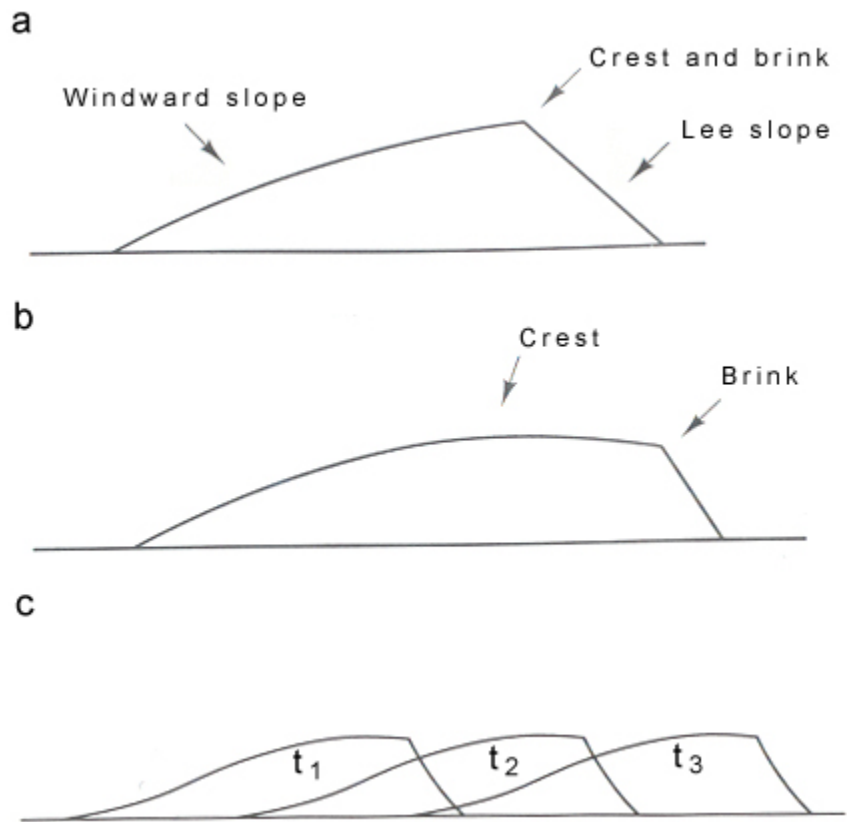


Figure 5.2. Cross-sectional dune shape and dune movement. Redrawn after Livingstone and Warren (1996).

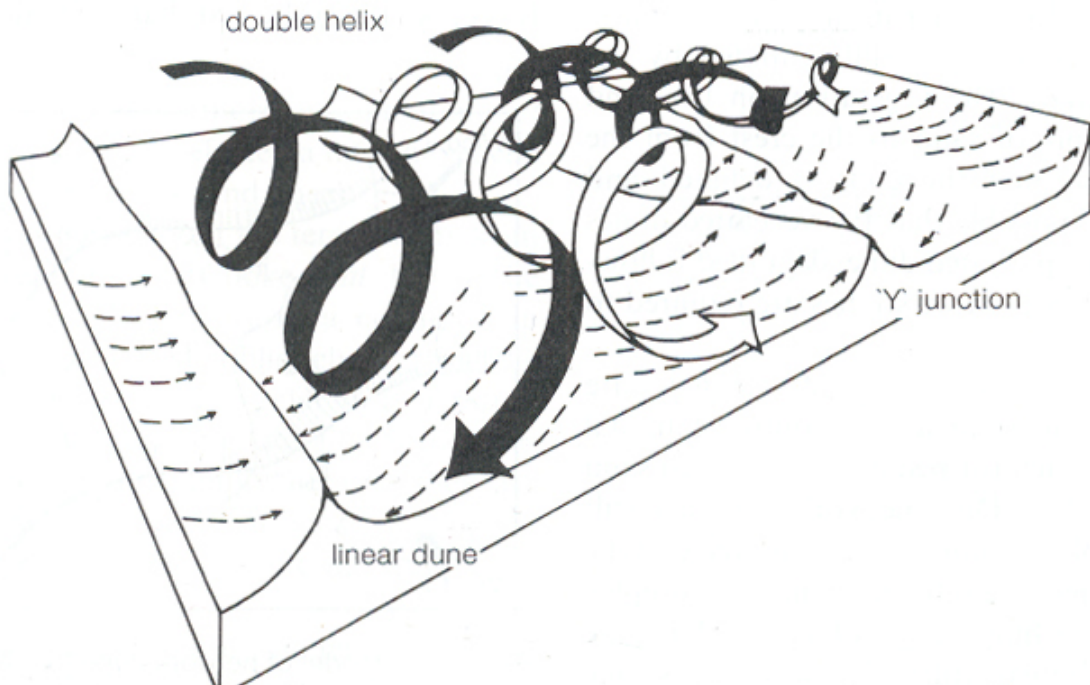


Figure 5.3. Hypothesis for linear dune formation in which a pair of thermally induced roll-vortices sweep sand from the interdune corridors onto the dune. After Livingstone and Warren (1996).

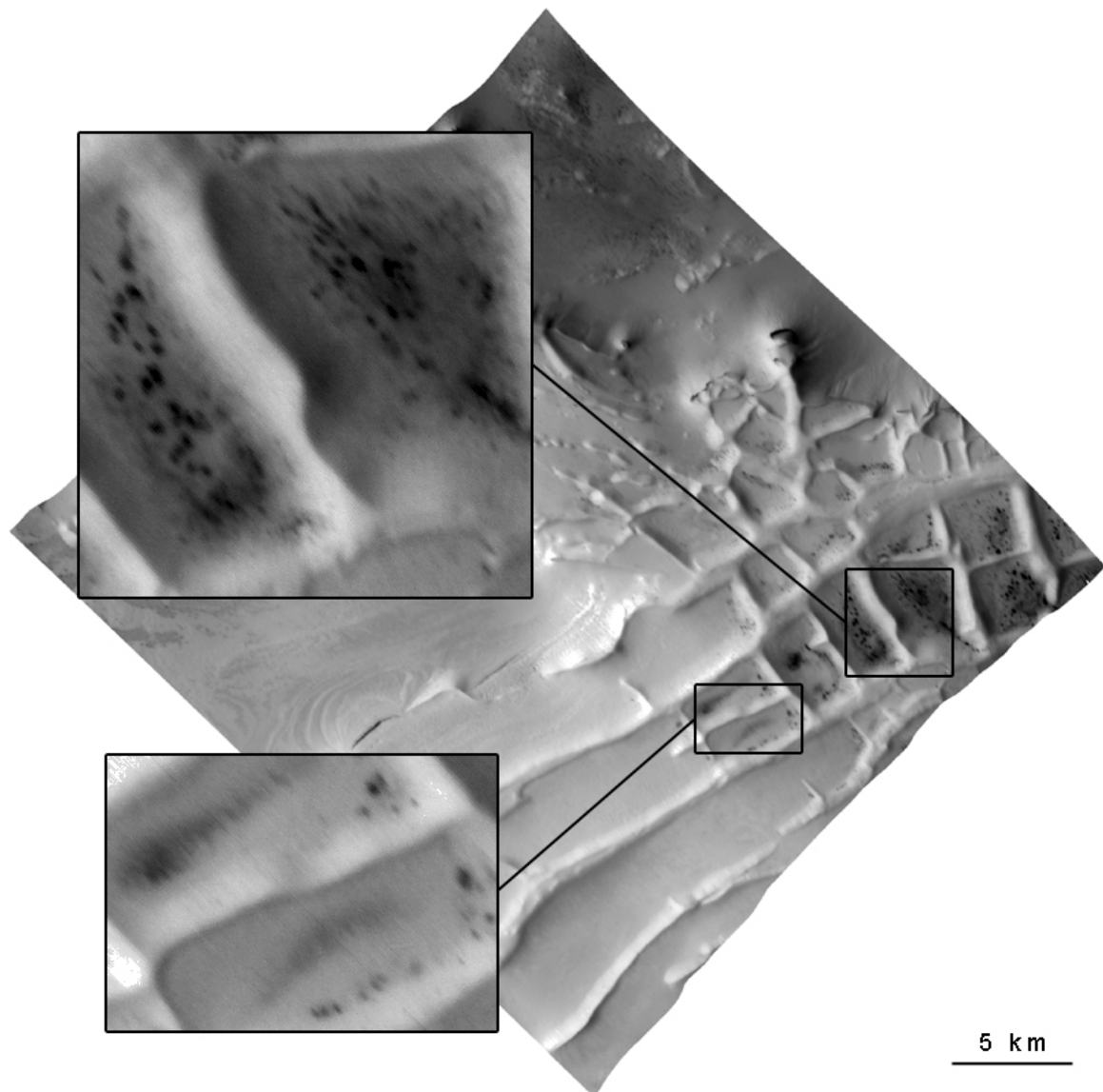


Figure 5.4. Example of two smooth curved crests of Inca City ridges.

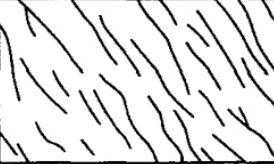
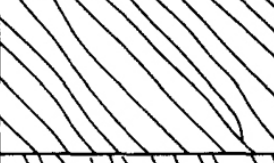
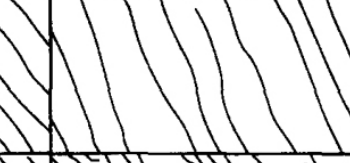
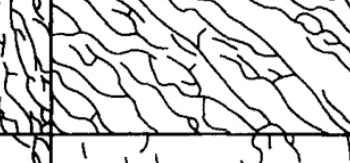
	General Description	Example Location	Planimetric Pattern		
			Example 1	Example 2	Example 3
1	Dunes parallel/sub-parallel, discontinuous occurring as short lengths (< 2km). Y-junctions uncommon and there are no transverse elements.	26° 49'S 21° 00'E			
2	Dunes parallel/sub-parallel and continuous for several km, few Y-junctions and no (or very rare) transverse elements. Those Y-junctions which do occur tend to form at the junction of two long dunes rather than as short spurs at the side of a dune. Occasional slip faces on crests but < 2m².	26° 42.57'S 20° 42.15'E			
3	Dunes parallel/sub-parallel and continuous for several km. Y-junctions common, both as parallel dunes merge and as short spurs < 600m on either side of dune. No slip faces on undisturbed dunes but may be common where grazing occurs.	26° 33.01'S 20° 31.42'E			
4	Linear dune network comprising large steep dunes and smaller gently sloping dunes. Larger dunes have broadly linear trend but are very sinuous. Small dunes tend to be orientated perpendicular to this trend. Small pans occur in deep interdune areas. Both types of Y-junction occur, Y-junctions and termini are common.	26° 26.84'S 20° 48.35'E			
5	No obvious linear trend and a chaotic hummocky appearance. Dune slopes shallow with very rounded crests. Dunes have low relief but occasional dunes up to 7 - 8m high. Very little interaction between dunes.	26° 08.74'S 20° 36.37'E			

Figure 5.5. Five classes of linear dunes occurring in the southwestern Kalahari desert, Africa. After Bullard et al. (1995).

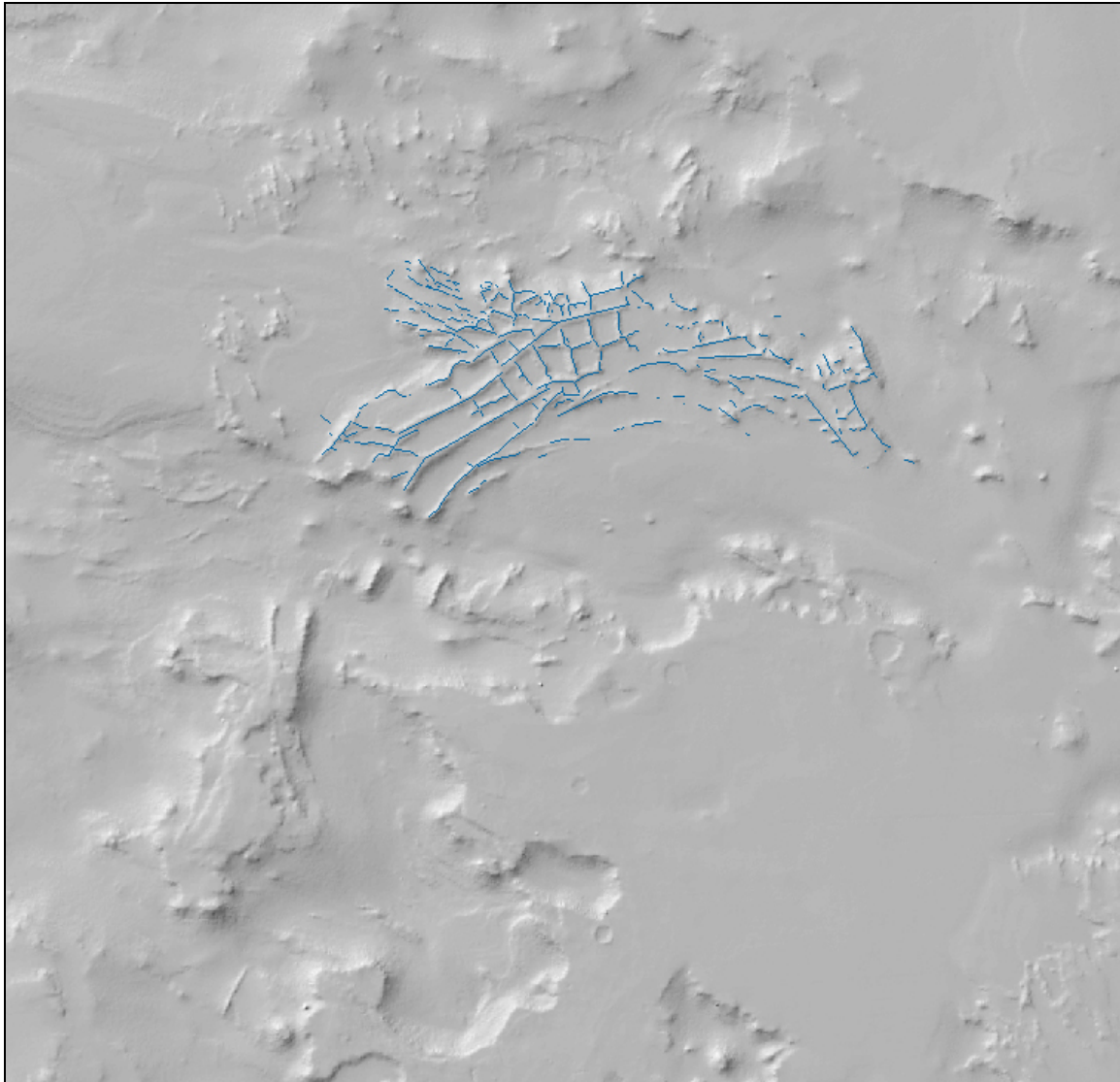


Figure 5.6. The Inca City ridges and the ridges in its vicinity.

Tables

Epoch	Division	Boundary age
Amazonian	Late	300-600 Ma
Hesperian	Early	2.9 – 3.3 Ga
	Late	
Noachian		
	Early	3.5 Ga
	Late	

Table 2.1. The Martian Timescale, after Hartmann and Neukem (2001).

Parameter	Value
Central Meridian	0°
Standard Parallel	-90°
Linear Unit	Meter
<i>Geographic Coordinate System:</i>	
Sphere radius	3396190 m
Angular Unit	Degree
Prime Meridian	0°

Table 3.1. Parameters of the South Polar Stereographic projection.

Image #	Resolution (m/pixel)	# GCPs	RMS (m)	RMS (pix)	Orientation
M04-00678	2.8	6	149.8	0.64	110.73
M14-02193-1	2.8	4	8.3	0.04	110.86
M14-00267	5.5	11	71.9	0.31	110.33
E11-00066	4.3	9	87.9	0.38	111.04
R08-01665	4.3	4	99.1	0.43	109.39
R07-01997	4.3	4	35.9	0.15	110.29
E07-00862	4.2	8	170.9	0.73	110.81
R08-00402	4.3	7	128.7	0.55	110.12
E09-01806	5.8	4	44.3	0.19	110.23
E10-03766	4.3	5	60.4	0.26	110.72
E11-01376	5.8	6	120.9	0.52	110.79
E07-01476	2.9	5	54.5	0.23	110.39
E06-01662	5.5	6	68.8	0.30	108.97
E05-00821	5.6	6	110.5	0.48	110.34
E04-01887	11.0	6	88.6	0.38	110.33
E07-00232	5.5	4	80.0	0.34	110.45
E07-00333	3.4	6	55.6	0.24	267.62
E09-02162-1	5.8	6	93.7	0.40	249.21
M09-05894	2.8	9	101.1	0.43	248.51

E07-00515	5.6	5	25.7	0.11	248.61
Image #	Resolution (m/pixel)	# GCPs	RMS (m)	RMS (pix)	Orientation

Table 3.2. Properties of the mosaic of MOC NA image slices. All 20 images were georeferenced using a first order transformation. Sixteen images have orientation around 110 and belong to Group A, the bottom 4 images belong to Group B.

Mission Subphases	Duration
AB1 through M04	September 1997 - August 1999
M07 through M12	September 1999 - February 2000
M13 through M18	March 2000 - August 2000
M19 through M23	September 2000 - January 2001
E01 through E06	February 2001 - July 2001
E07 through E12	August 2001 - January 2002
E13 through E18	February 2002 - July 2002
E19 through R02	August 2002 - February 2003
R03 through R09	March 2003 - September 2003

Table 3.3. Mission Subphases of the MGS orbiter and duration.

Appendix I – Acquisition of the MOC NA images.

Because the MOC Gallery contains many images, it is divided in 9 image collections of different periods (Table 3.3) spanning between September 1997 and September 2003. For each collection a map of the South Polar Region (Figure 3.18) can be retrieved which includes the ‘footprints’ of MOC NA images. Clicking on a footprint results in a new window where the subsequent image can be downloaded. Because of the low resolution of the map and the many ‘footprints’ present, simply selecting all the ‘footprints’ near Inca City on the map proved to be an incomplete method. Therefore the HTML file containing the map and the location of the MOC NA images was saved to disk and edited in a text editor so that the data became divided by tabulators and could be imported in Microsoft Excel. In Excel the distance between each image and Inca City was calculated. The images closest to Inca City were selected. This was repeated for each collection.

Appendix II – Calculating the Track Incidence angle.

Figure 3.19 illustrates the calculations of the Track Incidence angle (α_{ti}). A is the altitude of the MGS during image acquisition, B is the distance between the MGS and the location of the image center (Slant Distance) and R is the radius of Mars. A and B were obtained from the download page of image AB1-07908 in the MOC Gallery, A is 3222870 m and B is 4167300 m. The radius of Mars is 3396190 m. The following formula was used, which is a derivation of the standard ‘Law of Cosines’:

$$1. \quad R^2 = (R+A)^2 + B^2 - 2(R+A)B \times \cos(\alpha_{ti})$$

The formula was rearranged so α_{ti} could be determined:

$$2. \quad \alpha_{ti} = \arccos\left(\frac{R^2 - (R+A)^2 - B^2}{-2(R+A)B}\right)$$

This resulted in a Track Incidence angle for image AB1-07908 of $\sim 25.9^\circ$.

Appendix III – Importing the latitude and longitude of the MOC NA image slices into ArcMap.

Ancillary data for each MOC NA image can be obtained from the image download page in the MOC Gallery (Figure 3.12) containing the longitude and latitude of the image center. For all 87 images, these values, plus the image name were copied and paste into Microsoft Excel.

Figure 3.20 illustrates the calculations used to convert the latitude and longitude coordinates of the images into the South Polar Stereographic coordinate system. Angle A was determined:

1. $A = 90 - \text{'latitude of image center'}$.

Distance B is the radius of the sphere defined in the South Polar Stereographic projection (Table 3.1). This allowed for distance C to be calculated, with B 3396190 m:

2. $C = \tan(A) \times B$.

The last step involved calculating the X and Y values of the images in the South Polar Stereographic coordinate system:

3. $X = C \times \cos(90 + \text{'longitude of image center'})$

4. $Y = C \times \sin(90 + \text{'longitude of image center'})$

The Excel sheet was saved as a ‘dBase IV’ file with three columns, containing the image name, the X and the Y values, respectively, for each image. This file was imported into ArcMap using the ‘Add XY Data’ tool, which created a new layer containing the point data. In the ‘Label’ tab of the ‘Layer Properties’ window the label for the layer was turned on showing the image name at each point (Figure 3.21).